THE PENNSYLVANIA STATE UNIVERSITY
SCHREYER HONORS COLLEGE

DEPARTMENT OF BIOMEDICAL ENGINEERING

# Shear Effects on Blood-Protein Adhesion in Microfluidic Devices

SHANE WARD
SPRING 2021

A thesis
submitted in partial fulfillment
of the requirements
for a baccalaureate degree
in Biomedical Engineering
with honors in Biomedical Engineering

Reviewed and approved* by the following:

Keefe Manning
Associate Dean for Academic Affairs, Schreyer Honors College
Professor of Biomedical Engineering and Surgery
Thesis Supervisor

Meghan Vidt
Assistant Professor of Biomedical Engineering
Honors Adviser

Scott Medina
Assistant Professor of Biomedical Engineering
Thesis Reader

* Electronic approvals are on file.

# ABSTRACT

Left ventricular assist devices (LVADs) are an established method of surgical intervention for patients with heart failure. The implementation of these devices has led to significantly improved survival rate, yet the current generation of devices also cause increased risk of numerous secondary pathologies or complications. Pathological blood flow causes many patients to exhibit a poor ability to maintain hemostasis. This can lead to complications such as gastrointestinal bleeding, stroke, or device-mediated thrombosis. A common disorder prevalent in LVAD patients is acquired von Willebrand syndrome (AVWS), which causes dysfunction of the blood protein von Willebrand factor (vWF).

Recent studies have sought to understand the adverse effects of supraphysiological shear rates caused by a LVAD which impairs vWF function. Because vWF is an essential protein in shear-mediated clotting, it has been hypothesized that high shear rates cause excessive elongation and cleavage of vWF by the protein ADAMTS-13. Excessive cleavage of vWF results in the inability of vWF to adhere and recruit platelets at sites of vascular injury. This study was designed to understand how vWF and platelet adhesion to various substrates is driven by shear rates consistent with physiological circulation as well as the high shear of LVAD flow.

This study hypothesizes that there exists a threshold at which von Willebrand factor is the primary cause of platelet adhesion, rather than integrin-surface interaction. Evidence of increased platelet adhesion due to hypershear is exhibited. Presence of ADAMTS-13 in pathological shear rates is shown to diminish the effect of vWF in platelet recruitment and even decrease platelet adhesion at lower shear rates.

TABLE OF CONTENTS

LIST OF FIGURES

LIST OF TABLES

## ACKNOWLEDGEMENTS

I would like to thank my thesis advisor Dr. Manning for his continued support and guidance. Being a member of your lab has been an absolute pleasure. Thank you to the many others in the Artificial Heart Lab who have helped me along the way and taught me so much. Thank you to Connor Watson who has made this possible through his constant support and leadership. You have greatly helped me cultivate my own intellectual curiosity. Thank you to Stefano Rizzo for all your help. To my professors and other members of the Penn State community who have helped me grow intellectually, I thank you. Finally, I would like to thank my mother Robin, father John, sister Abby, and brother Kellan. Thank you to my entire family for continually supporting me in whatever I may do and always pushing me to challenge myself.

# Chapter 1

# Clinical Need

## Ventricular Assist Devices

Rates of heart failure continue to grow in the United States, currently affecting over 6.5 million patients in the United States alone[1]. A five-year survival rate of around 50 percent makes heart failure a demanding problem to solve[1]. Surgical intervention routes for heart failure include transplantation or mechanical circulatory support (MCS). Transplantation is the ideal therapeutic solution, but a number of limiting factors often necessitate MCS implantation. Limitations for heterologous transplantation include limited donor supply and strict criteria for transplant candidacy, such as age, absence of comorbidities, and lack of alternative options[4,5]. These constraints and improving survival rates in MCS, make MCS an increasingly relied upon therapy[2,3].

Left ventricular assist devices (LVADs), accounting for 93% of MCS implants, are now the main long-term treatment for heart failure[6]. Based on rates of heart failure and the current selection criteria, at present, there are between 125,000 and 250,000 candidates for VAD implantation in the United States[2,7]. These candidates may use these devices as a bridge to transplantation or recovery because the devices, by working alongside the native heart, relieve multiple symptoms of heart failure[7]. However, due to improved long-term survival, the largest growing use is as a destination therapy by the population of candidates ineligible for transplant[2,7].

First generation LVADs used volumetric displacement to mimic pulsatile flow of the native heart. These devices were unsuitable for long-term application due to poor durability. Failure usually occurred within two years of implantation and presented a major risk to the patient[2,8]. These pumps created further problems due to their size and weight, which greatly reduced the candidate pool for implantation[2,8]. The

introduction of continuous flow (CF) LVADs made these devices more widely accessible to smaller men, women, and children due to its small size and greatly reduced rates of device failure[2,8]. The advantages of CF devices resulted in a sharp decline in use of pulsatile devices. Today, up to 99% of implanted LVADs operate under continuous flow[6].

Use of an LVAD is often accompanied by various other secondary pathologies that can develop in a patient including infection, device-mediated thrombosis (DMT), stroke, or bleeding events. Many of these developed pathologies cause readmission to hospitals greatly affecting survival rates and patient quality of life. Around half of patients return to the hospital within a month and in the first-year post-implantation, patients, on average, need emergency assistance 7 times[9]. Bleeding, accounting for 35% of adverse events, is one of the most common causes of recurrent hospitalization[2,6,10]. Increased incidence of adverse bleeding events coincided with the switch to CF devices[2,10].

The incidence of bleeding in these CF LVADs has multiple factors. Anti-coagulation with warfarin, used to mitigate thromboembolic events, present a factor for bleeding yet the correlation between continuous flow and bleeding events also relies on the pump itself. The impeller of the LVAD, which drives the flow of blood, alters blood flow from physiological conditions by applying supraphysiological shear stresses, which can result in significant blood trauma[8]. This trauma causes hemolysis and alters the function of various coagulation factors, including platelets and von Willebrand factor[8].

## Acquired von Willebrand Syndrome

The ability to maintain hemostasis can be affected by LVAD implantation. The adoption of CF LVADs was accompanied by increased risk of both too much and too little coagulation[2,10,19,20]. Due to the decreased ability to maintain hemostasis, bleeding events are very common in CF device patients[2,10]. Although some had hypothesized this was due to the necessity for anticoagulation treatment to prevent

pump thrombosis, anticoagulant treatment cannot account for the totality of decreased function[21]. Instead, the dysfunction may be predominately caused by the conditions the pump imposes.

Acquired von Willebrand syndrome (AVWS) is one such disease affecting hemostasis in which scarcity or absence of high molecular weight vWF multimers cause decreased ability to bind GPIb sites on platelets[22,23]. This is thought to be a primary cause of bleeding events in patients with LVADs. In studies of the CF LVAD HeartMate II, almost all patients had AVWS and all those that had major bleeding events had AVWS with low to absent high molecular weight multimers[22,23].

vWF dysfunction in these patients is thought to be caused by the high shear rates present due to the VAD impeller. This is supported by increased incidence of bleeding events in patients with stenosis[24], decreased dysfunction with decreased rotor speed in the HeartWare VAD[21], and decreased vWF deficiency in devices designed to minimize shear[20]. The effect high shear rate has on hemostasis is explained by the function of ADAMTS-13 under these conditions. Rates faster than physiological speed have been shown to increase ADAMTS-13 cleavage by increased exposure to A2 domain sites[25,28,29]. Recent studies have found enzymatic proteolysis increases significantly after a critical shear rate of 6,000 $s^{-1}$ [28, 29]. This is supported by decreased amounts of high molecular weight vWF in CF LVAD patients yet higher amounts of medium and low molecular weight vWF[19].

Both axial and centrifugal CF devices induce regions of shear flow greater than 100,000 $s^{-1}$, much larger than physiological shear rate and the critical shear rate for ADAMTS-13 enzymatic activity[49]. These incredible speeds cause vWF to elongate much faster and to a greater extent than that seen under physiological conditions. The resulting lack of high molecular weight multimers results in decreased platelet binding causing the bleeding events observed in patients with AVWS[16].

# Chapter 2

# Coagulation

## Coagulation Cascade

Hemostasis is maintained *in vivo* by the coagulation cascade, depicted in Fig. 1-1, which uses several procoagulant proteins and inhibitors[11,32,33]. Primary hemostasis creates a platelet plug at the site of vascular injury[11,32]. This begins with exposed collagen binding to various platelet glycoprotein receptors[31,36,37]. This activates platelets causing a change in shape and a release of their granules[36,37]. Platelet activation can then also occur by bound platelet secretions, local prothrombotic factors like tissue factor, or shear activation[31,36,37]. Fibrinogen or vWF bound to GPIIb/IIIa crosslinks and stabilizes these platelets[31,36,37].

Secondary hemostasis is initiated to form crosslinked fibrin around the platelet plug for a stabilized thrombus[11, 32]. This begins along either the intrinsic or extrinsic pathway, both ending in the common pathway, which ultimately converts fibrinogen to fibrin[11,32,34]. The intrinsic pathway begins with the activation of factor XII by exposure to endothelial collagen at a site of endothelial damage to become factor XIIa[11,32,34]. Factor XIIa catalyzes factor XI into factor XIa [32,34,35]. Factor XIa activates factor IX[32,34,35]. Finally, factor IXa activates factor X to factor Xa to end the intrinsic pathway[32,34,35]. As the cascade continues, the concentration of each successive factor gets greater than the previous[32,34].

Alternatively, the extrinsic pathway is activated by the release of tissue factor, which occurs after vascular injury or tissue trauma[11,30,33]. This similarly reaches the activation of factor X, which begins the common pathway[11,30,32,35]. Tissue factor activates factor VII to factor VIIa[30,32,33]. Factor VIIa activates factor X to factor Xa[11,30,32,35].

After either pathway activates factor X, factor Xa, with cofactor factor V, activates factor II (prothrombin) to factor IIa (thrombin) [32,34,35]. When either pathway causes the activation of factor II, the

intrinsic pathway is reinforced by positive feedback to factors V, VII, VIII, XI, XIII[32]. Thrombin cleaves fibrinogen into fibrin. Fibrin is crosslinked, with the help of Factor XIII, to form a mesh for stabilization of the platelet clot [32,35].

Various procoagulants also activate inhibitors which work to regulate the expression of proteins to localize clotting to the site of injury[11, 32]. Notably, thrombin, while working as a procoagulant, also activates plasminogen to plasmin which degrades the fibrin mesh and produces antithrombin[32]. Antithrombin inhibits the activation of prothrombin and factor X[30,32]. Activated proteins C and S inhibit the activation of factor VIII or factor V [30,32].

Drugs introduced into circulation can inhibit processes within the cascade. Warfarin, an anticoagulant prescribed to LVAD patients, acts as a vitamin K antagonist[38,39]. Several important factors require vitamin K for their procoagulant functions[38,39]. Use of warfarin inhibits such factors, including factors II, VII, IX, and X[38,39]. Alternatively, heparin can be administered to bind with antithrombin to inhibit thrombin and factor X[46].

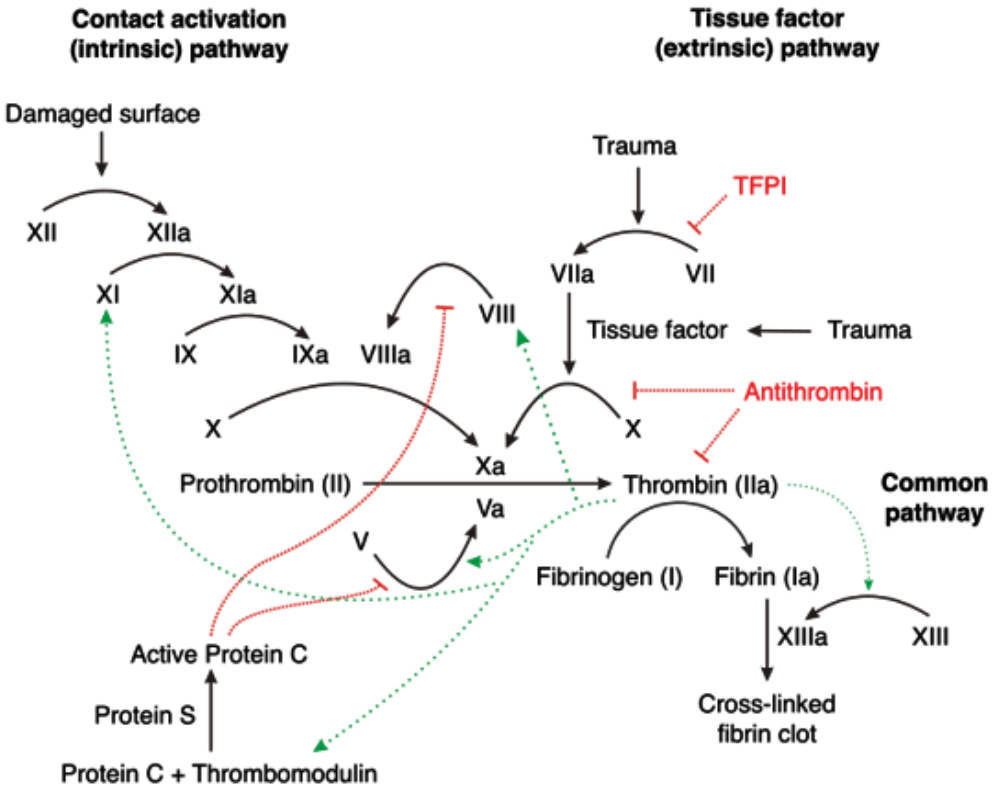


**Figure 2-1: Procoagulants of coagulation cascade which lead to a fibrin clot[30].**

## Shear Dependent Coagulation

Von Willebrand factor, a large, heterogeneous, adhesive glycoprotein, plays a key role in shear dependent hemostasis[13,14,15]. vWF is synthesized in endothelial cells (EC) and megakaryocytes as globular monomers, then stored as a tightly furled multimer[13]. vWF is released into plasma and EC activation by thrombin, histamine, etc. causes further increase in vWF release into subendothelial matrix and plasma[13,14]. vWF also plays a key regulatory role by preventing the degradation of factor VIII and shear-mediated binding of other proteins at sites of vascular injury or high shear[13,15].

Shear stress is essential in both the function and regulation of vWF. vWF multimers, typically present in a coiled conformation, can be elongated based on shear to expose various binding and cleavage sites[13,14,15]. vWF has binding sites for heparin, collagen, ADAMTS-13, factor VIII, and platelet

glycoproteins Ib (GPIb) and IIb/IIIa (GPIIb/IIIa)[14]. The A3 domain of vWF recognizes and binds collagen to anchor the protein to the endothelium, allowing elongation under stress[13]. Such elongation exposes the A1 domain in a force dependent manner[13,14]. These domains are shown below in Fig. 2-2. At lower shear, platelets are marginated and roll slowly along the vessel walls which allows for arrest at the site of injury. Under high shear, most platelet interactions, including vWF-GPIIb/IIIa binding, break down[14,31]. However, vWF-GPIb binding remains efficient at higher shear due to exposure of repeated A1 domains due to elongation[31]. This complex is shown in Figure 2-3. After a threshold of 500-800 $s^{-1}$, vWF A1 domain binding to GPIb is the only functional interaction to arrest platelets at a site of injury[14,15,31]. Due to the increased likelihood of elongation for larger multimers, high molecular weight vWF are predominantly responsible for platelet-binding activity[16].

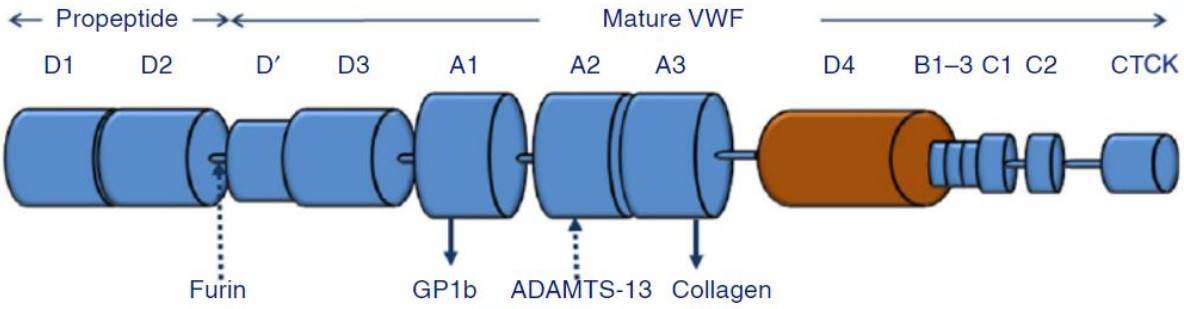


**Figure 2-2: Domains of vWF for collagen, GPIb (platelet), and ADAMTS-13 binding13.**

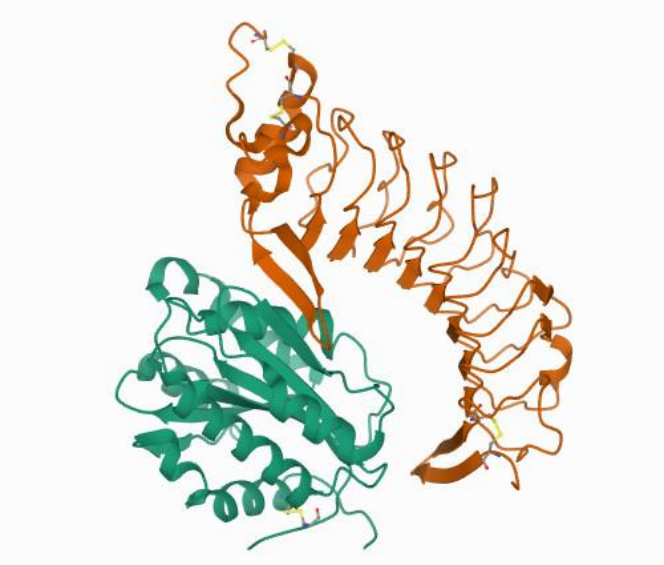

**Figure 2-3: vWF A1 domain structure (green) bound to GPIb (orange).[51]**

Due to the quick association and dissociation of the vWFA1-GPIb bond, a permanent bond between these binding sites is unable to be formed under high shear rates[17, 18]. The GPIb site, which causes platelet adhesion to collagen under low flow, is unable to fully arrest platelets under high flow conditions. Instead, platelets translocate over vWF strands until a stronger, more permanent bond is formed, such as GPIIb/IIIa to fibrinogen[17,18]. This bond is more irreversible compared to the GPIb bond yet takes longer to form, making it difficult for binding to occur in flow conditions in which the platelets pass the fibrinogen binding sites too quickly[18]. Therefore, vWF plays an essential role in shear-mediated coagulation as its platelets are slowed by continually reversible attachments to GPIb, which allows more permanent arrest by GPIIb/IIIa despite high shear rates[17,18]. Stabilization then occurs by platelet binding to fibrinogen and consequential platelet aggregation[15]. However, the efficacy of GPIb's transient binding to platelets declines at rates above 900 $s^{-1}$ [18].

vWF formation requires regulation to prevent pathophysiological binding of platelets forming undesired thrombosis. Left unchecked, vWF can cause Thrombotic Thrombocytopenic Purpura Extension, where patients experience excess coagulation[12,15]. Circulatory protein ADAMTS-13 cleaves vWF to regulate vWF lengths and prevent adverse coagulation[12, 14, 15]. vWF extension from stress and binding of

the A3 domain to collagen causes a force dependent elongation of the A2 domain, exposing the cleavage site for the enzyme ADAMTS-13[12,14]. Cleavage causes detachment from the endothelium and a loss of shear-dependent binding function[14].

## Objective

The goal of this study is to quantify the effect of shear rate on vWF and platelet binding in conditions relevant to mechanical circulatory support. Using isolated vWF with and without ADAMTS-13, and whole blood with stained platelets, adhesion in a microfluidic channel will be quantified through immunofluorescence microscopy to understand how high shear rates may affect the coagulation abilities of patients with AVWS. Additionally, platelet adhesion will be studied to understand the impact of vWF binding on the ability to recruit other blood proteins. Shear effects will be studied in microfluidic channels sealed to glass slides and coated with collagen.

# Chapter 3

# Methods

## Channel Fabrication

Polydimethylsiloxane (PDMS) channels were fabricated for the study of blood protein adhesion. Dimensions for the geometry were inputted into Solid Works ® (SolidWorks Corp., Waltham, MA) and used for creation of the master mold at Politecnico di Milano. The master mold was created using photolithography. This starts by spin coating an SU-8 photoresist (Thermo Fisher Scientific, Waltham, MA) on a Silicon wafer. SU-8 was spun on the wafer for 30 seconds at 1000 rpm to create an even layer of photoresist. Exposure to UV light was controlled by a mask, tailored to the desired geometry. UV exposure crosslinks the photoresist to solidify into desired geometry. Unexposed regions fail to crosslink and were washed off. Photolithography steps are shown in Fig. 3-1.

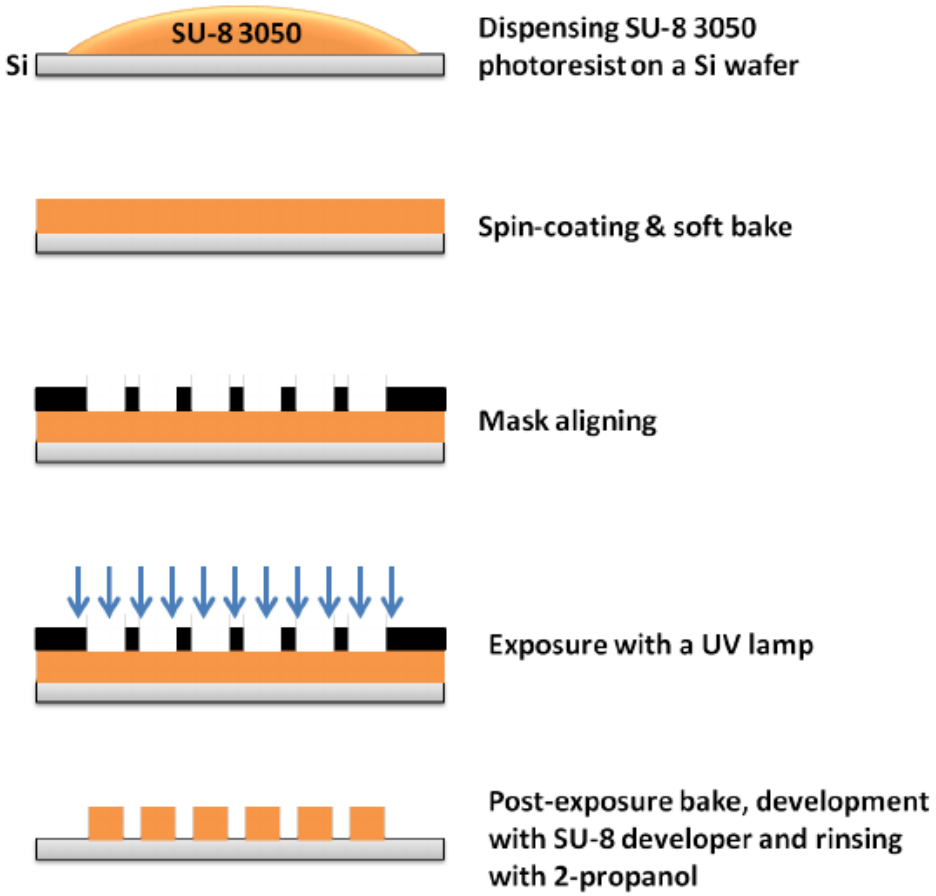


**Figure 3-1: Steps for creation of master mold using photolithograpy[40].**

After creation of the reusable mold, PDMS channels can be created by soft lithography. Sylgard-184 silicone elastomer and curing agent (Dow Chemical Company, Midland, MI) were mixed at a 10:1 ratio for 5 minutes. The mixture was placed in a degassing chamber to remove any bubbles. Once all bubbles have been removed, the PDMS mixture was poured over the mold and degassed again. After, the channel was cured on a hot plate at 150˚C for 15 minutes or in a 37˚C hot room for 24 hours until solid. The inlet and outlet of the channel were punched with 1 mm holes.

PDMS channels were attached to glass slides (VWR, Radnor, PA) using plasma oxidation. Glass slides and channels were placed in plasma cleaner (Harrick Plasma Inc, Ithaca, NY) for 10 minutes. Oxidizing introduces hydrophilic silanol groups (SiOH) to the surfaces to increase surface wettability[41]. When silanol groups of the PDMS and glass contact each other, a covalent bond is formed to seal the two surfaces[41]. This process is shown in Fig. 3-2.

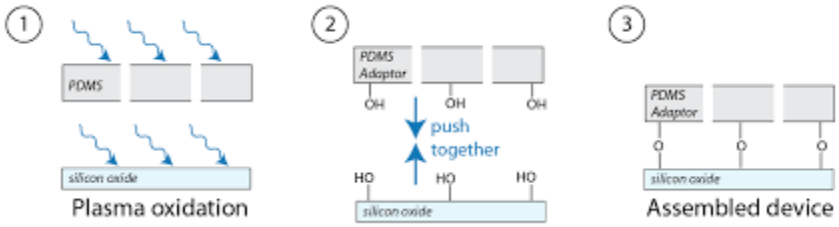


**Figure 3-2: Plasma treatment of PDMS and glass for channel creation[41].**

Channel geometry for μPIV was characterized by a backward facing step (BFS) and a crevice. The backward facing step has a rapid expansion, doubling in width. The initial channel is 200 μm x 10 μm with an expansion to 400 μm x 10 μm. From this point forward this will be referred to as the "flat backward facing step" due to its small height. Figure 3-3 shows the geometry of this channel.

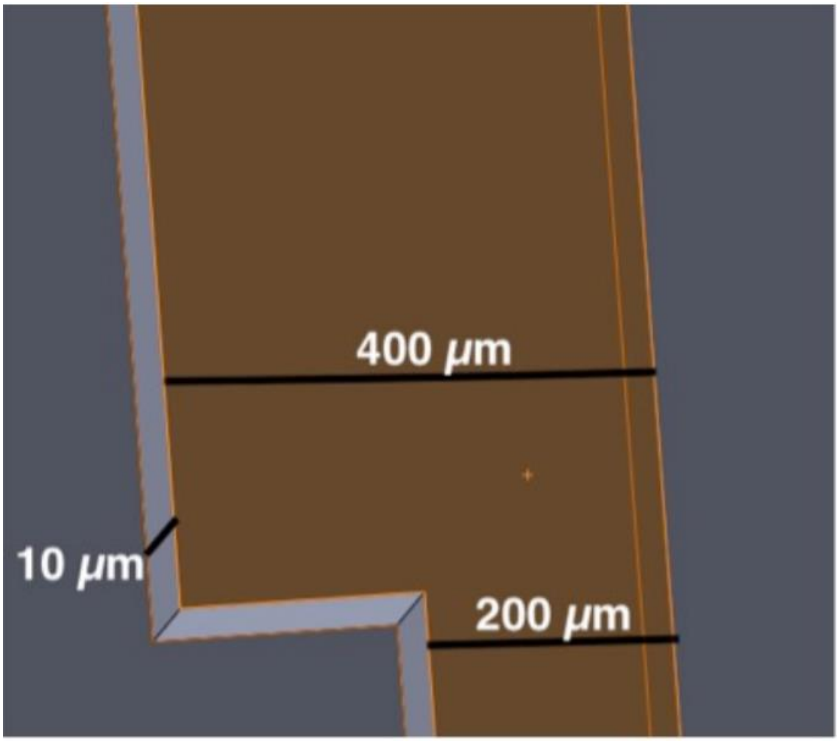


**Figure 3-3: Channel geometry for the flat backward facing step. Inlet is at the bottom and outlet is on the top.[26]**

The crevice channel has a 400 μm x 10 μm main channel with a 122 μm long crevice extending 90 μm from the main channel. This geometry is shown in Figure 3-4.

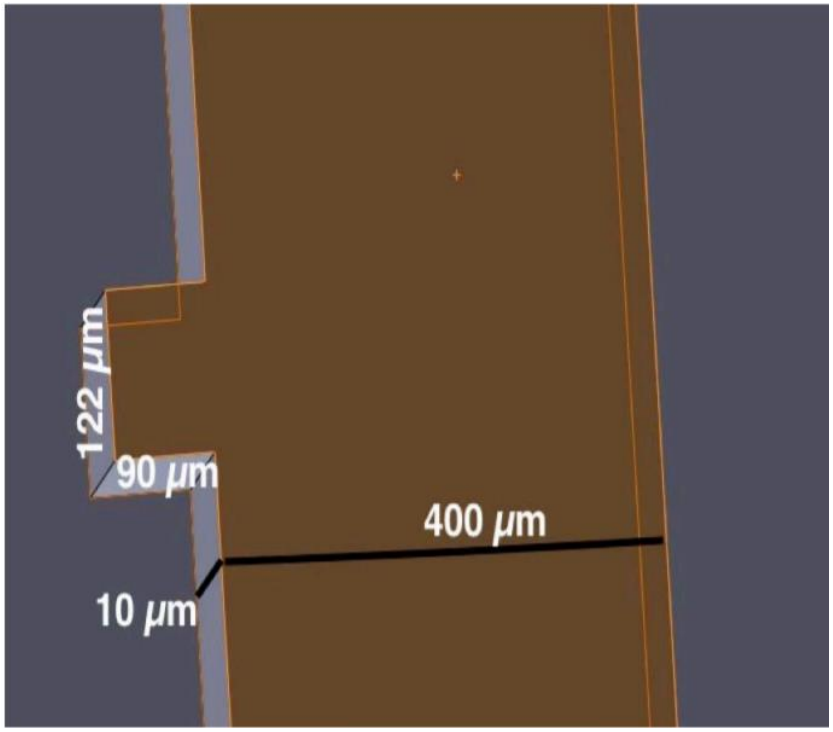


**Figure 3-4: Channel geometry for the crevice channel. Inlet is at the bottom and outlet is on the top.**[26]

The channels used for immunofluorescent microscopy were characterized by a backwards facing step. Multiple dimensions of backward facing steps were used for this study. All channels had a point of rapid expansion where the channel doubled in width. All channels have a constant height of 50 μm. The channels had initial widths of 200 μm, 400 μm, and 600 μm. These will henceforth be referred to as "small", "medium", and "large," respectively. Geometries of the channels can be seen in Fig. 3-5.

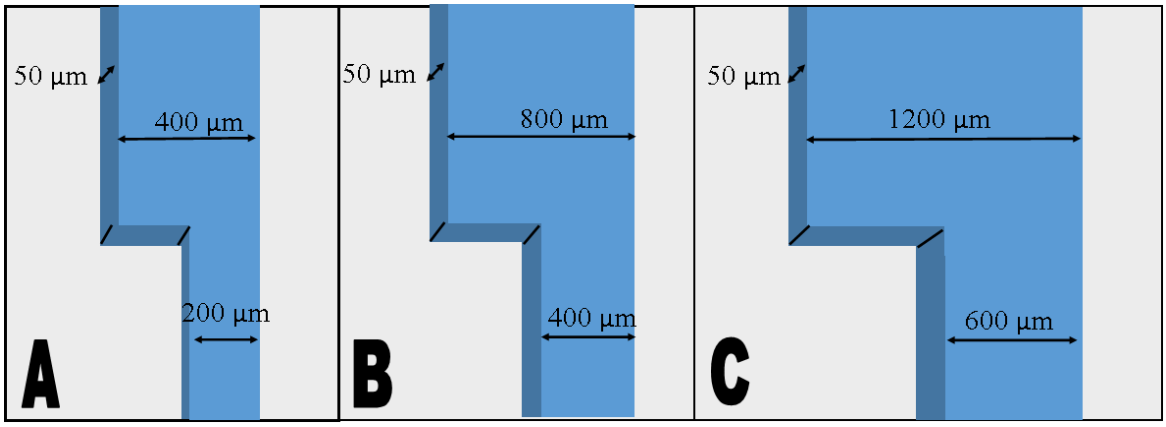


**Figure 3-5: Geometries of PDMS channels for (A) small, (B) medium, and (C) large backward facing step channels (not to scale).**

## Micro-Particle Image Velocimetry

Micro-particle image velocimetry (µPIV) was used to quantify fluid flow within microfluidic channels. Using an Nd:YAG 532 nm laser (New Wave Research, Inc., Fremont, CA), two distinct emissions were pulsed at known time interval ΔT. Tracer particles (Thermo Fisher Scientific, Waltham, MA) were seeded in the fluid of interest and follow pathways consistent with the surrounding fluid. These particles excited from laser emissions at 540 nm and emitted a longer wavelength of light at 560 nm. Wavelengths were separated to image only the longer wavelength of the particles using a 532 nm filter cube (Nikon, Melville, NY) with a 532 laser bandpass (49907-C183941).

A Laserpulse synchronizer (TSI, Shoreview, MN) controlled a Powerview 4MP-HS CCD camera (TSI, Shoreview, MN) to capture images during periods of laser illumination. Imaging of the channel was performed by attaching the camera to a Nikon Eclipse TE300 microscope (Nikon, Melville, NY) with a Plan Fluor 20X (Nikon, Melville, NY) objective. The setup of µPIV is shown in Figure 3-6.

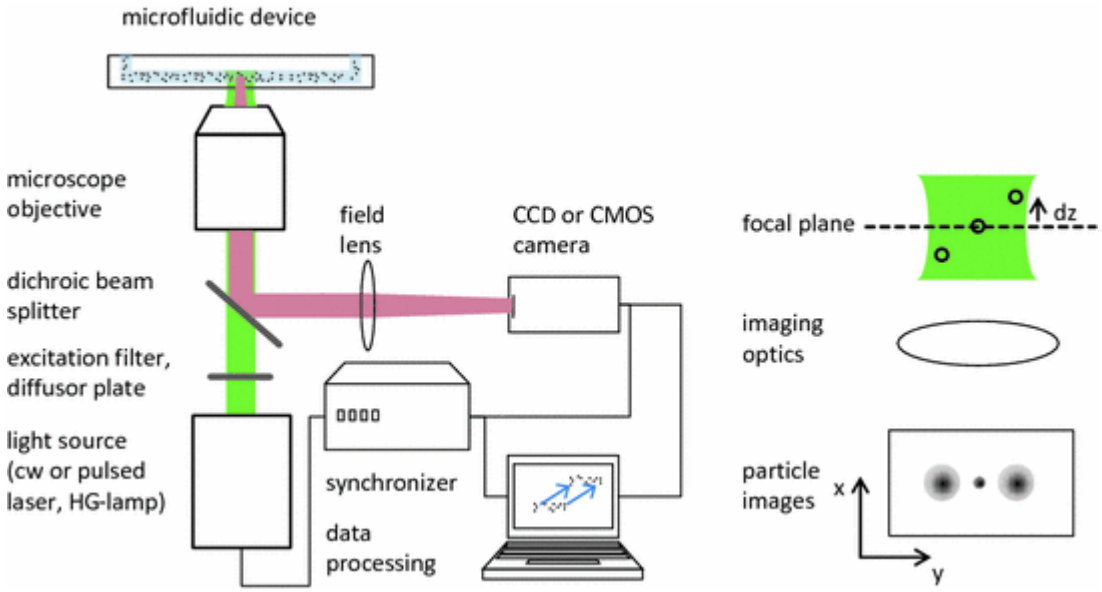


**Figure 3-6: Setup of µPIV equipment for image acquisition [42].**

Multiple image pairs were captured at the same known time interval. Using the distance traveled between frames and the known interval, Insight 4G (TSI, Shoreview, MN) can calculate an average velocity for each interrogation window. For accurate measurements, particles traveled 1/3 the interrogation window between frames in the region of interest. To ensure the proper distance traveled ΔT is calculated using Equation 1, where Q is volumetric flow rate, A is cross-sectional area of the channel, and x is the length of the interrogation window. After vector calculation, values were imported to Tecplot (Tecplot, Inc., Bellevue, WA) for post-processing. The delta T used for each flow condition and channel is shown in Table 3-1.

$$\frac{Q}{A}\,\Delta T = \frac{1}{3}\,x \tag{1}$$

**Table 3-1: Time intervals used to image various flow rates, channels, and regions of flow for µPIV.**

| *Channel type* | *Flow Rate* | | *ΔT (µs)* |
|---|---|---|---|
| **Crevice** | 1 | Main channel | 350 |
| | | Zoomed | 1400 |
| | 10 | Main channel | 140 |
| | | Zoomed | 560 |

| | | | |
|---|---|---|---|
| | 20 | Main channel | 560 |
| | | Zoomed | 2240 |
| **BFS** | 1 | Main channel | 350 |
| | | Zoomed | 1400 |
| | 10 | Main channel | 70 |
| | | Zoomed | 120 |
| | 20 | Main channel | 140 |
| | | Zoomed | 560 |

## Computational Simulations

Fluent (ANSYS® Workbench 2019 R1; ANSYS, Inc.) was used to create computational fluid dynamics models to assess the shear rates of the channels. Laminar flow was used to describe the physics due to low Reynolds numbers in the channels at the conditions used. Models consisted of 10x10x3.125 µm elements. Boundary conditions were a normal inlet flow rate equal to the rate of interest and an outlet with pressure set to 0 Pa. Fluid properties were set to 1 cP viscosity and 1000 $kg/m^3$ density to mimic vWF and di$H_2O$ solutions. The solution method was Green-Gauss Node Based spatial discretization and SIMPLE pressure-velocity coupling scheme. Simulations stopped once residuals reached $10^{-6}$. Simulation results are analyzed on CFD-post (ANSYS® Workbench 2019 R1; ANSYS, Inc.), to obtain the needed shear rate values, and the velocity profiles which will be used to validate the model.

## Fluid Preparation and Perfusion

The fluids used to perform this study were isolated vWF with di$H_2O$, vWF and ADAMTS-13 with di$H_2O$, whole human blood and whole blood with ADAMTS-13. The isolated vWF fluid was made by combining vWF (Haematologic Technologies, Inc., Essex, VT) with di$H_2O$ for a concentration of 12 µg/mL. The same concentration was used for the vWF and ADMATS-13 fluid. ADAMTS-13 was added at a concentration of 1 ug/mL. For whole blood with additional ADAMTS-13, blood was supplemented with 0.5 ug/mL of ADAMTS-13.

Fluids were perfused through the channels using a KD Scientific syringe pump (KD Scientific Inc., Holliston, MA). The syringe pump was used to control the shear rate by varying the volumetric flow rate. This relationship is defined by Equation 2, where Q is volumetric flow rate, h is the height of the channel, w is the width of the channel, and $\dot{\gamma}$ is the shear rate.

$$\dot{\gamma} = \frac{6Q}{h^2 w} \tag{2}$$

## Indirect Immunofluorescence Microscopy

Immunofluorescence microscopy (IFM) was used to quantify the adhesion of blood proteins. In the first experiments, images were acquired using indirect immunofluorescence microscopy with a specific primary antibody and a fluorescent secondary antibody. A rabbit polyclonal anti-human vWF primary antibody (ab6994, Abcam plc) was used to specifically bind vWF. A fluorescent secondary goat anti-rabbit antibody (Alexa Fluor 488 – conjugated, ab150077, Abcam plc) nonspecifically bound and fluoresced.

Prior to experimentation, channels were coated in collagen (100 μg/mL) and incubated for 1 hour. A PBS wash at 10 μL/min washed the unadhered collagen after the incubation period. The solution of interest (vWF/$H_2O$ solution or vWF/ADAMTS-13/$H_2O$ solution) was perfused at the experimental rate for two minutes. After vWF perfusion and adherence, the channel was washed with primary antibody (1:500 dilution) for 5 minutes at 5 μL/min followed by a 5-minute PBS wash to remove unbound antibody. Secondary antibody (1:500 dilution) was introduced to the channel at 5 μL/min for 5 minutes to adhere to rabbit antibodies, which are bound to the vWF. This was followed by a final 5-minute PBS wash. Channels used for these experiments are taken in the straight inlet sections of the backward facing step channels described previously.

## Direct Immunofluorescence Microscopy

Fluorescent antibodies were combined with the fluid to label proteins of interest. Platelets were labeled with a green fluorescent, lipophilic dye, 3,3' dihexyloxacarbocyanine iodide ($DiOC_6$) (Thermo Fisher Scientific, Waltham, MA). $DiOC_6$ excites at 482 nm and emits at 504 nm. An Olympus C31991 U-N41001 HQ:FITC (4) filter cube (Olympus Corporation, Shinjuku City, Tokyo, Japan) was used with a ThorLabs FL 488-10 excitation filter and HQ535/50 X 43813 emission filter. Figure 3-7 shows the pathways of light through the filters during fluorescence microscopy to acquire images of fluorescent antibodies.

The dyes for both indirect and direct immunofluorescence experiments were excited by a X-cite mini LED light source (Olympus Corporation, Shinjuku City, Tokyo, Japan) through an Olympus IX71 inverted microscope (Olympus Corporation, Shinjuku City, Tokyo, Japan). An Olympus DP4 CMOS camera was attached to the microscope to acquire images of the fluorescence after filtration of the wavelength. Images were acquired using CellSens (Olympus Corporation, Shinjuku City, Tokyo, Japan) software. The focal plane of the microscope was adjusted to capture the entirety of the depth of the channel. The depth was small enough that all proteins were in view. Brightfield images of the channel were acquired in the same position as reference for the boundaries of the channel.

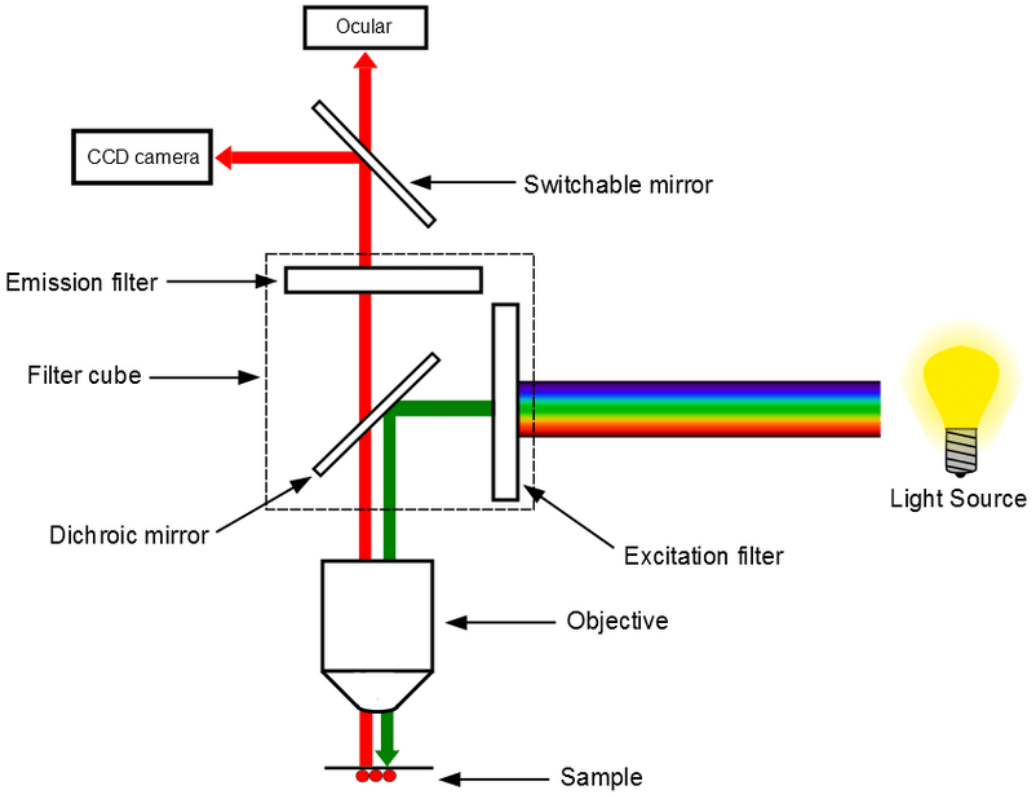


**Figure 3-7: IFM light pathways used to acquire images [43].**

Channels were cleaned and coated with collagen (100 µg/mL) before experiments. To clean after plasma treatment and attachment to glass slides, PDMS was exposed to UV light for 30 minutes. 80% ethanol was perfused through at 10 µL/min for an initial wash. The channels were then washed with a Tris-NaCl buffer (pH 7.4) at 20 µL/min for one minute. Collagen (100 µg/mL) was then injected into the outlet for 1 min. The channels were incubated for 1 hour at room temperature then washed again with the Tris-NaCl buffer. Channels were then stored at 4˚C until used.

## Image Analysis

CellSens software was used to remove the background noise from the images. Acquire indirect IFM images were then processed in ImageJ (National Institutes of Health, Bethesda, MD). Conversion into 8-

bit images allowed for thresholding to differentiate background from adhered protein to create a binary image. Images processed in ImageJ were analyzed using a custom MATLAB (MathWorks Natick, MA) script provided in Appendix A. The results give the percent of surface area covered in particles.

The direct IFM images were processed in FIJI (National Institutes of Health, Bethesda, MD). All time points for individual channels and conditions were processed together. Backgrounds were removed using the built-in function to reduce noise then images were made binary. The particles were analyzed by the software and total area covered was compared to the area of the channel to give percent of surface area covered by fluorescence. Figure 3-8 shows an example of a processed image.

**Figure 3-8: Example of a processed image.**

Statistical comparisons between groups were compared via ANOVA testing. Two-tailed t-tests were used to compare between averages. Significance was determined by an $\alpha$ level of 0.05.

## Shear-Platelet Adhesion Direct IFM Experiment

Platelet adhesion with various applied shear rates in whole blood were studied. $DiOC_6$ was combined with whole blood at a concentration of 0.2 μL/mL. All blood samples used were drawn from a human subject through an approved IRB protocol. Various volumetric flow rates were perfused through varying width collagen-coated channels to achieve experimental shear rate conditions. The rates and

channels used are shown in Table 3-2. Physiological shear rates of 1,000 $s^{-1}$ and 1,500 $s^{-1}$ were studied as well as supraphysiological rates of 5,000 $s^{-1}$ and 10,000 $s^{-1}$. Previous studies have found several regions of flow with shear rates at or well over 10,000 $s^{-1}$ for multiple centrifugal LVAD designs[50]. Fluids were perfused at experimental rates for 2 minutes to mimic previous indirect immunofluorescence vWF studies. Images were taken every two minutes to see platelet adhesion in real time.

**Table 3-2: Channel and flow rate used to generate target shear rate.**

| *Shear Rate* | *Channel Used* | *Volumetric Flow Rate* |
|---|---|---|
| **1,000 $s^{-1}$** | Large BFS | 15 µL/min |
| **1,500 $s^{-1}$** | Medium BFS | 15 µL/min |
| **3,333 $s^{-1}$** | Large BFS | 50 µL/min |
| **5,000 $s^{-1}$** | Medium BFS | 50 µL/min |
| **10,000 $s^{-1}$** | Small BFS | 50 µL/min |

### ADAMTS-13 Effect on Platelets Direct IFM Experiment

The effect of ADAMTS-13 on platelet adhesion under varying shear rates were studied using whole blood. Blood was taken from human subjects through an IRB approved protocol. $DiOC_6$ was combined with whole blood at a concentration of 0.2 µL/mL of blood. Half of the blood samples were supplemented with ADAMTS-13 at 0.5 µg/mL of whole blood. Blood was perfused through a medium backwards facing step channel. Channels were cleaned and coated with collagen as previously described. Each sample was flown with varying shear rates controlled by a syringe pump as described previously. Samples were collected for n=3 for each condition. The volumetric rates and channels used to create shear rates are detailed in Table 3-3. Images were taken at 0, 1, 3, and 5 minutes to image adhesion in real time.

**Table 3-3: Channels and flow rates used to achieve target shear rates.**

| *Shear Rate* | *Channel* | *Flow Rate* |
|---|---|---|
| **1,000 $s^{-1}$** | Medium BFS | 10 μL/min |
| **5,000 $s^{-1}$** | Medium BFS | 50 μL/min |
| **10,000 $s^{-1}$** | Medium BFS | 100 μL/min |

# Chapter 4

# Results

## Micro-Particle Image Velocimetry

The velocities within channel geometries are shown in μPIV. Figure 4-1, Figure 4-2, and Figure 4-3 show velocity vector fields (in m/s) for a channel with a 90 μm x 122 μm crevice for flow rates of 1 μL/min, 10 μL/min, and 20 μL/min, respectively. The figures also show vector fields and streamlines within the crevice taken at a larger delta T more characteristic of flow within the slower moving region.

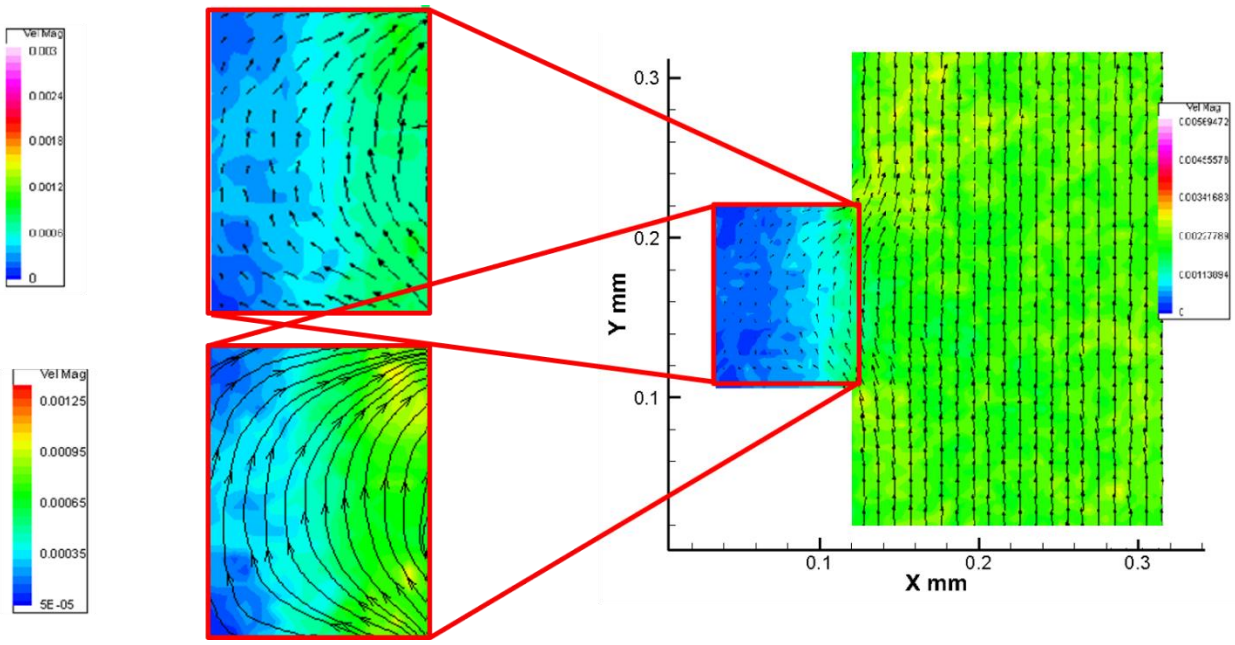


**Figure 4-1: Micro-PIV for a crevice in 1 μL/min flow of di$H_2O$ with velocity vectors and streamlines within the crevice.**

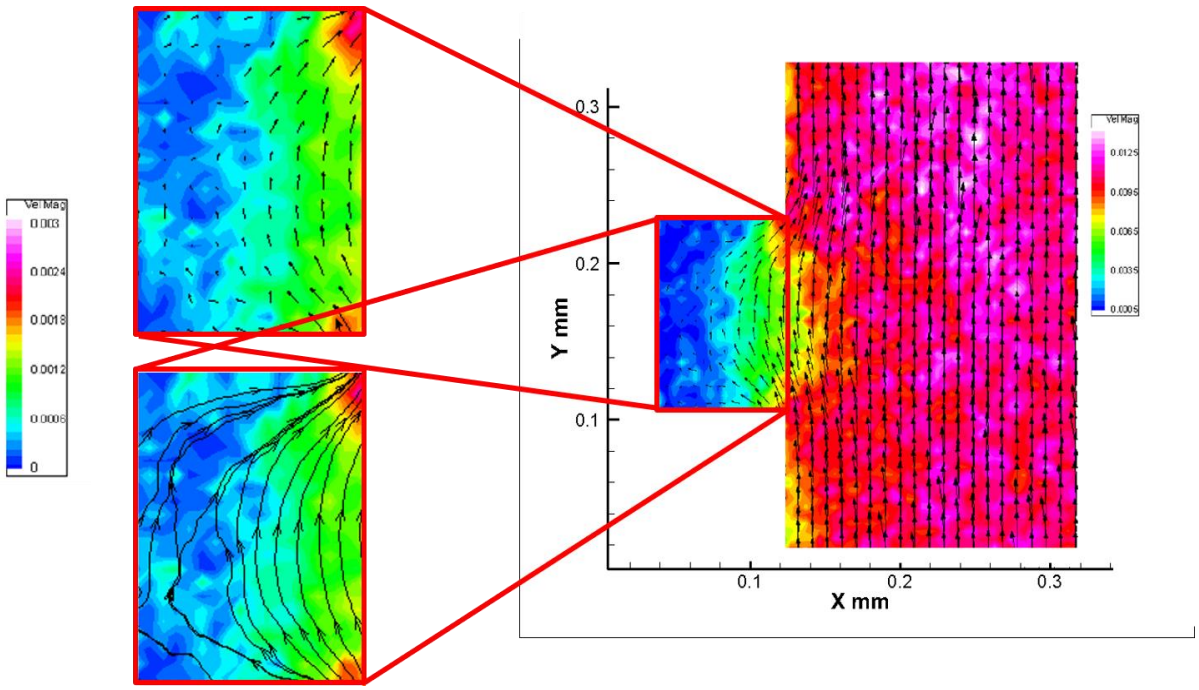


**Figure 4-2: Micro-PIV for a crevice in 10 µL/min flow of di$H_2O$ with velocity vectors and streamlines within the crevice.**

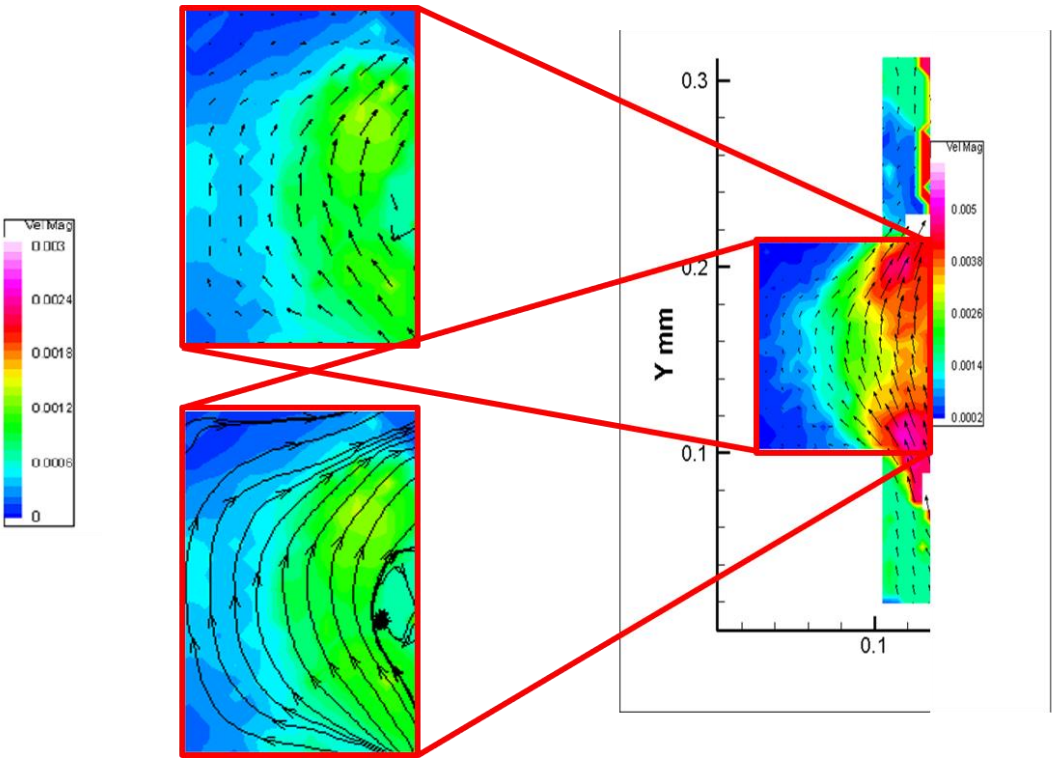


**Figure 4-3: Micro-PIV for a crevice in 20 µL/min flow of di$H_2O$ with velocity vectors and streamlines within the crevice.**

Figure 4-4, Figure 4-5, and Figure 4-6 show velocity vector fields (in m/s) at the rapid expansion of a backward facing step for 1 μL/min, 10 μL/min, and 20 μL/min, respectively. Velocity vectors and streamlines at the far corner of the expansion are also shown for a delta T characteristic of slow flow in those regions.

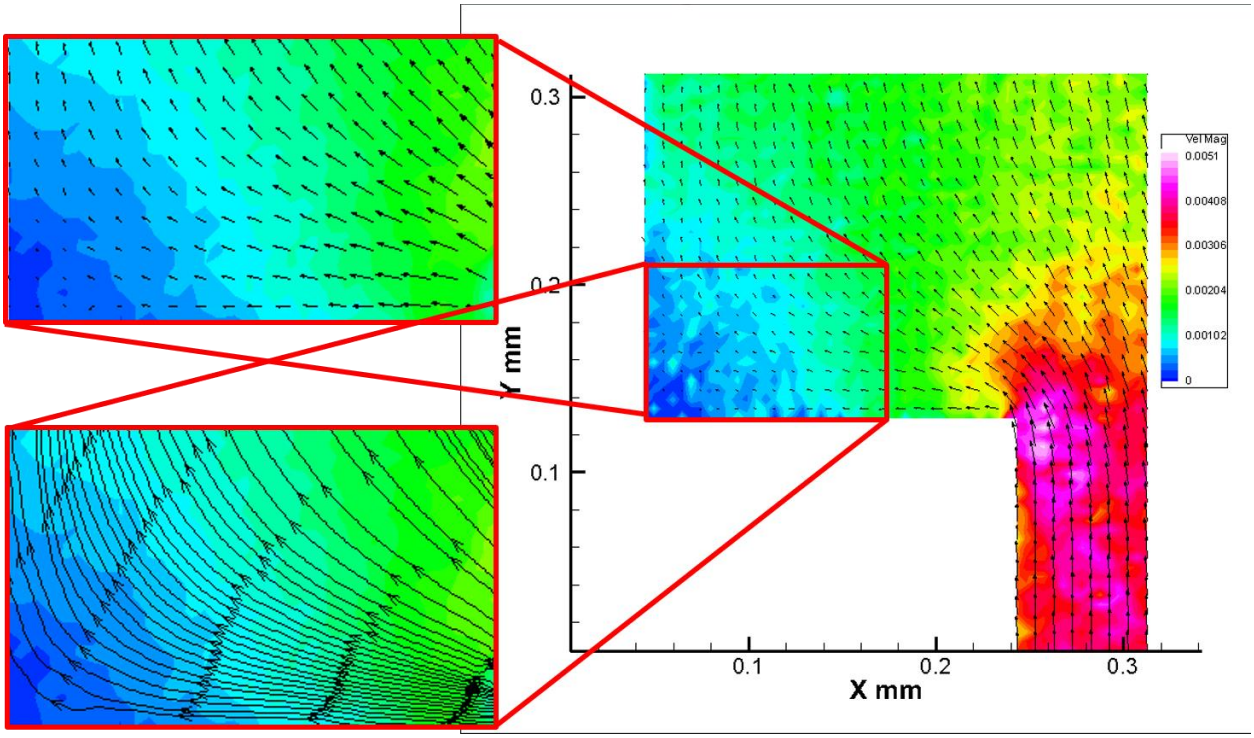


**Figure 4-4: Micro-PIV for a backward facing step in 1 μL/min flow of di$H_2O$ with velocity vectors and streamlines at the expansion.**

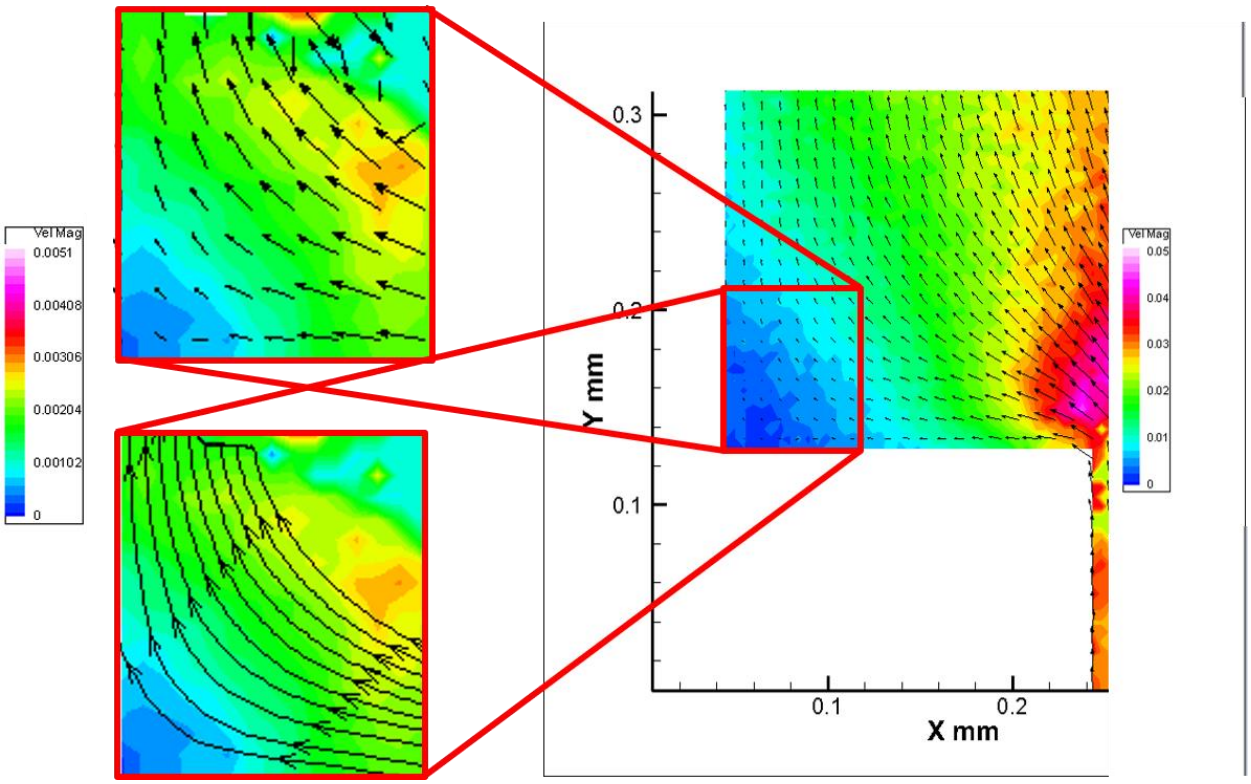


**Figure 4-5: Micro-PIV for a backward facing step in 10 μL/min flow of di$H_2O$ with velocity vectors and streamlines at the expansion**

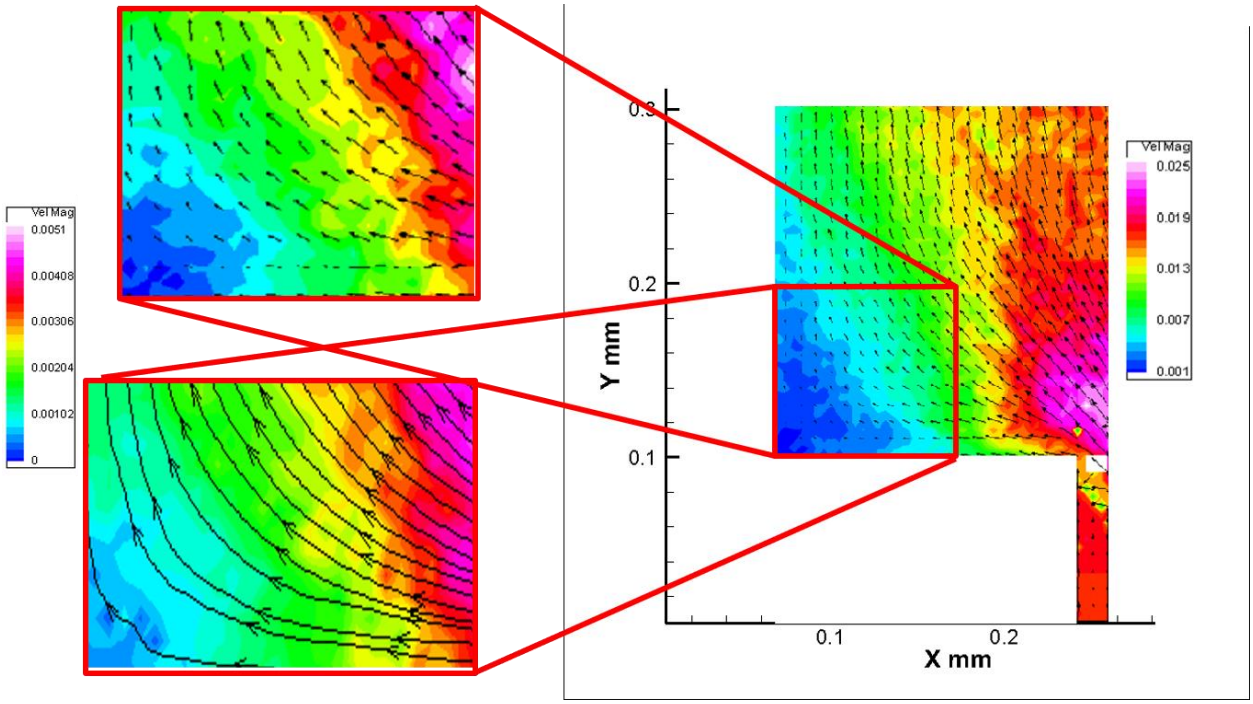


**Figure 4-6: Micro-PIV for a backward facing step in 20 µL/min flow of di$H_2O$ with velocity vectors and streamlines at the expansion**

Figures 4-7 through 4-9 show μPIV velocity fields for the small, medium, and large backward facing step channels at 15 μL/min. Velocity vectors at the far corner of the large channel were too slow to register a velocity.

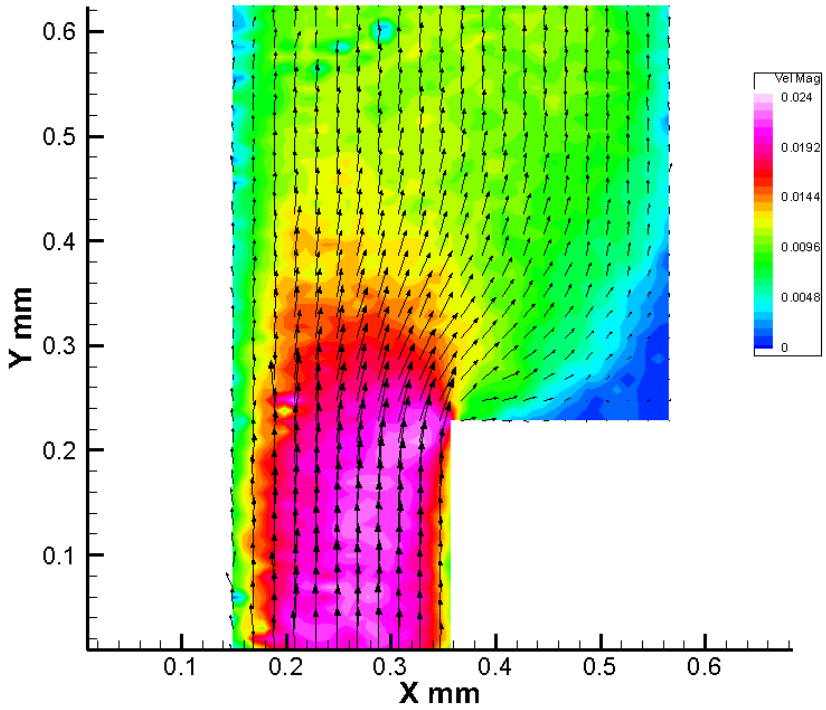


**Figure 4-7: Micro-PIV velocity vectors for the small channel at 15 μL/min.[47]**

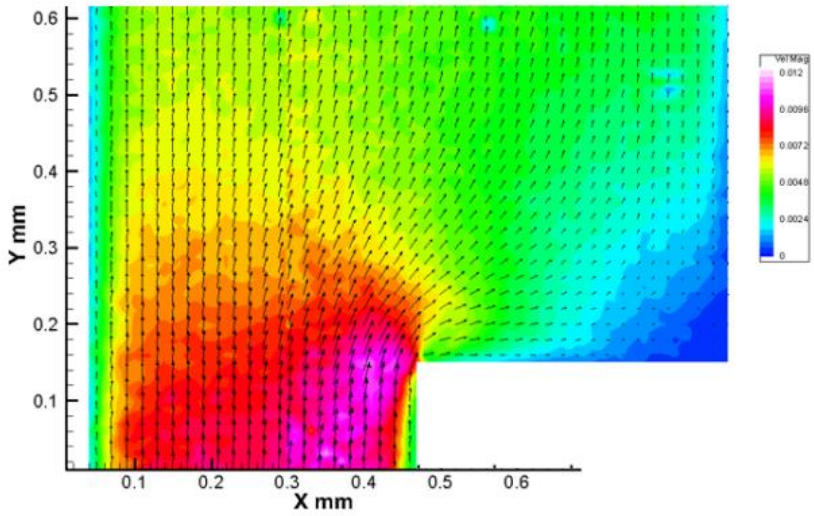


**Figure 4-8: Micro-PIV velocity vectors for the medium channel at 15 μL/min.[47]**

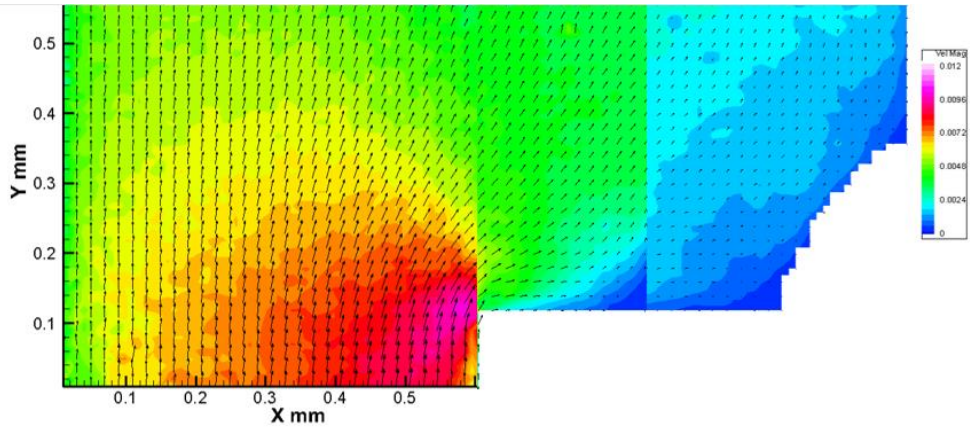


**Figure 4-9: Micro-PIV velocity vectors for the large channel at 15 μL/min.[47]**

## Computational Simulations

Velocity profiles across the channel at the expansion in the computational study were compared to PIV data. Figure 4-10 shows how the computational results match the PIV data for small, medium, and large channels at 15 μL/min. The relative errors for the small, medium, and large channels were 2.84%, 1.27%, and 7.48% respectively.

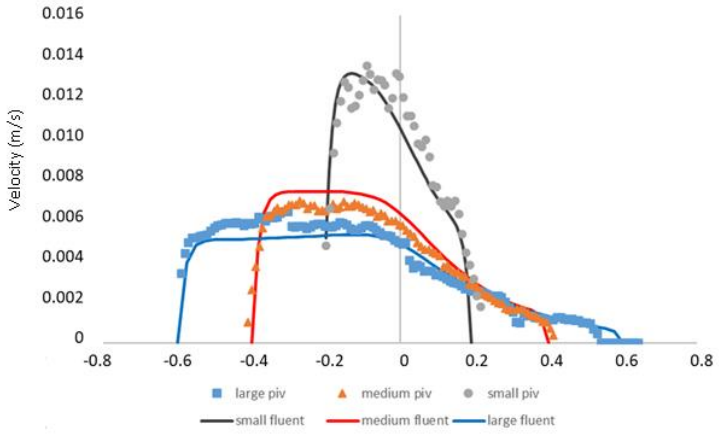


**Figure 4-10: Velocity profiles at the expansion for the small, medium, and large channels. Solid lines show ANSYS fluent results interpolated by MATLAB. Points show PIV data. [47]**

## Indirect Immunofluorescence Experiments

For the indirect immunofluorescence experiments, a solution of 12μg/mL of human vWF in di$H_2O$ was used to perfuse the channels. 1μg/mL of ADAMTS-13 was added to solutions for comparison. Shear rates of the different sized channels are shown in Table 4-1.

**Table 4-1: Average shear rates at Q= 50 μL/min within different sized channels.**

| *Channel* | *Average Shear Rate* |
|---|---|
| **Small (200 μm x 50 μm)** | 10,000 $s^{-1}$ |
| **Medium (400 μm x 50 μm)** | 5,000 $s^{-1}$ |
| **Large (600 μm x 50 μm)** | 3,333 $s^{-1}$ |

Figure 4-11 shows raw images collected via immunofluorescence microscopy. Bright blue spots show adhered vWF. Some noise was seen due to the presence of unadhered fluorescent secondary antibody. Adhesion was clearly distinguishable from noise and thus, easily removed through thresholding. These example images are taken at 25 μL/min in straight channels.

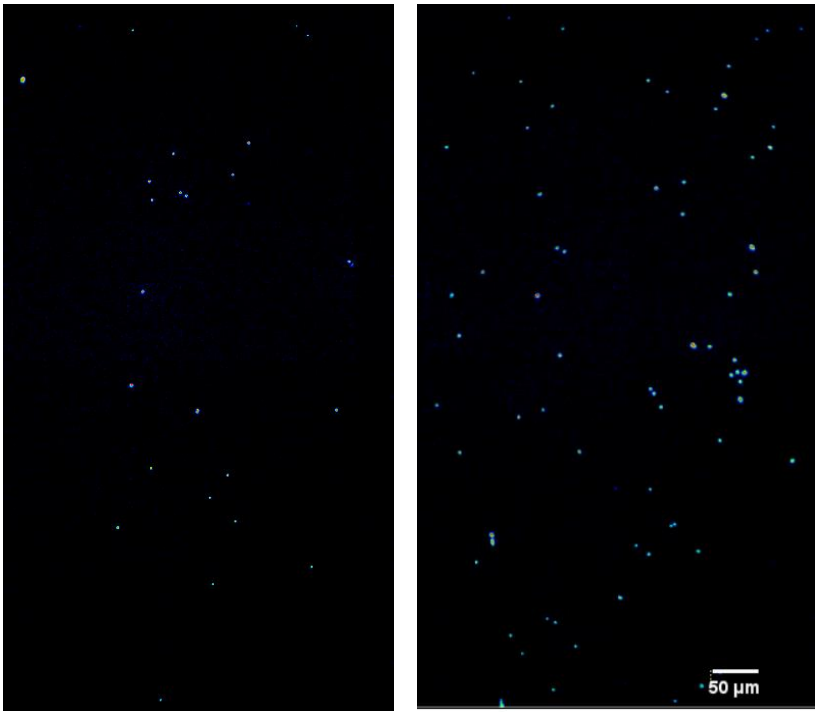


**Figure 4-11: Raw images of vWF adhesion in straight channel after two minutes of flow at 25 μL/min**

Figure 4-12 shows the percent area covered after two minutes of perfusion of the solution with only vWF and di$H_2O$ at 50 µL/min. Mean values for the percent area covered are shown in Table 4-2. A single factor ANOVA found statistically significant differences in adhesion between shear rates with only vWF (p=0.00049).

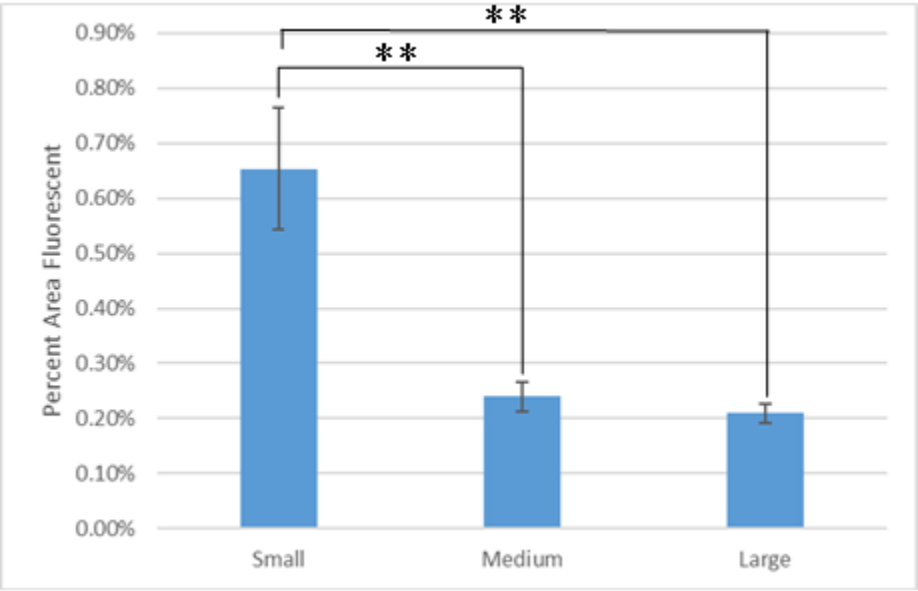


**Figure 4-12: Fluorescence coverage in three different sized channels after 2 minutes of vWF and di$H_2O$ flow at 50 µL/min.**

**Table 4-2: Percent area fluorescent for small, medium, and large channels**

| *Channel Size* | *Mean* | *SEM* |
|---|---|---|
| **Small** | 0.632% | 0.111% |
| **Medium** | 0.239% | 0.026% |
| **Large** | 0.245% | 0.017% |

Figure 4-13 shows the percent of area with fluorescence after perfusion of vWF and ADAMTS-13 in solution at 50 µL/min. The differences seen for adhesion with ADAMTS-13 are not statistically significant (p=0.503).

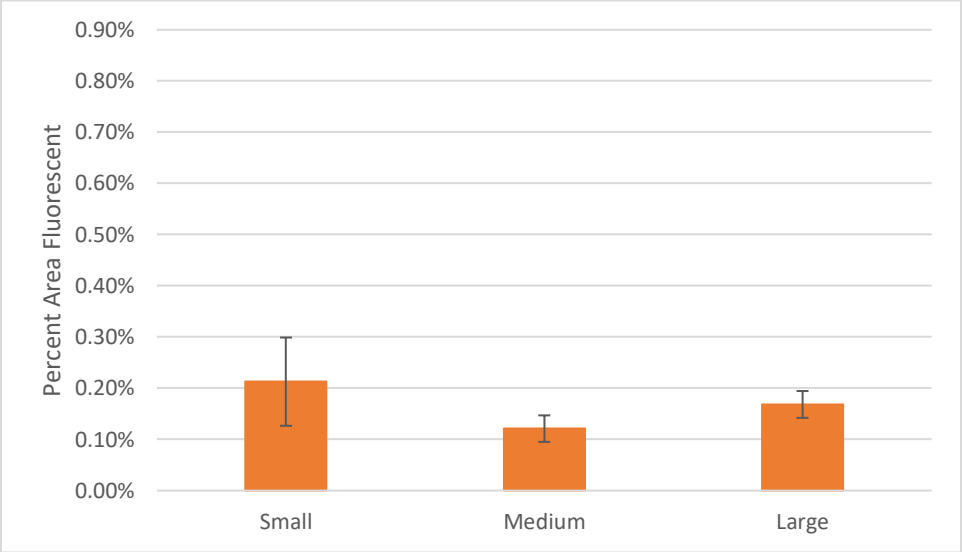


**Figure 4-13: Fluorescence coverage in three different sized channels after 2 minutes of vWF with ADAMTS-13 and di$H_2O$ flow at 50 µL/min.**

**Table 4-3: Percent adherence mean and standard error for vWF with ADAMTS-13**

| *Channel Size* | *Mean* | *SEM* |
|---|---|---|
| **Small** | 0.213% | 0.086% |
| **Medium** | 0.121% | 0.026% |
| **Large** | 0.168% | 0.026% |

Figure 4-14 shows the fluorescence for all 3 channels and both fluids together. Using a two tailed unpaired t-test ($\alpha$=0.05), the presence of ADAMTS-13 decreased the area with adhered vWF by a statistically significant amount in each channel ($p_{small}$=0.0056, $p_{medium}$=0.0012, $p_{large}$=0.0476).

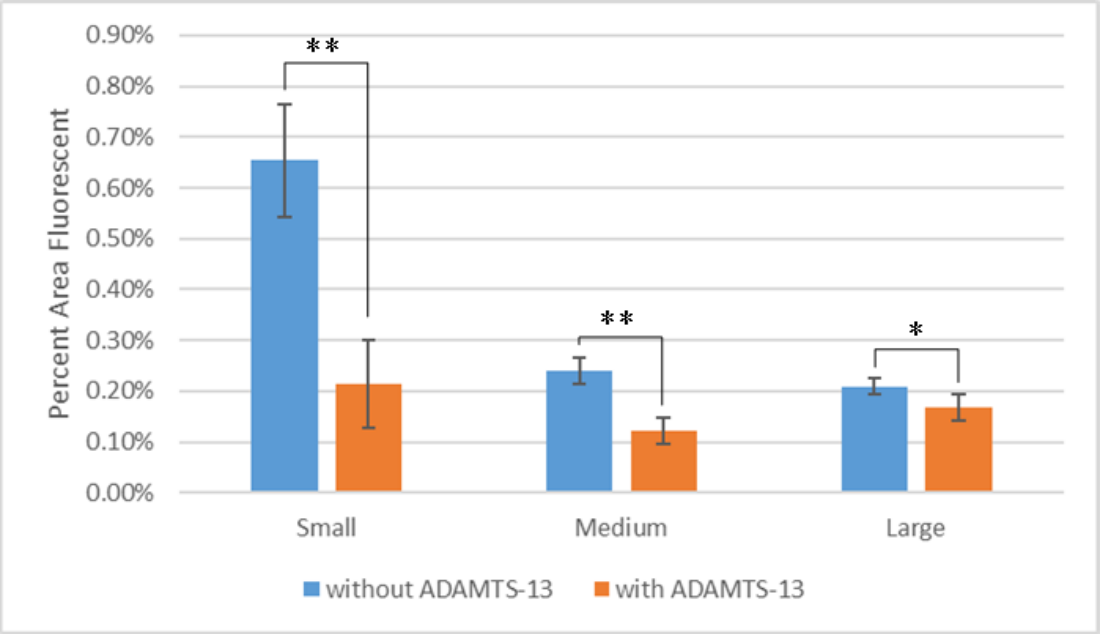


**Figure 4-14: Comparison of vWF adherence with and without ADAMTS-13 in small (10,000 $s^{-1}$), medium (5,000 $s^{-1}$), and large (3,333 $s^{-1}$) straight channels.**

## Shear-Platelet Adhesion Direct IFM Experiment

Figures 4-15 through 4-19 show the platelet adhesion over time for each shear rate: 1,000 $s^{-1}$, 1,500 $s^{-1}$, 3,333 $s^{-1}$, 5,000 $s^{-1}$, and 10,000 $s^{-1}$, respectively. All data points have an n=5. Averages and standard error bars at the time point for the given shear rate are shown. Figure 4-20 shows sample images of platelet deposits over time. These images start before the perfusion of fluids and continue with images at 30 second increments until two minutes.

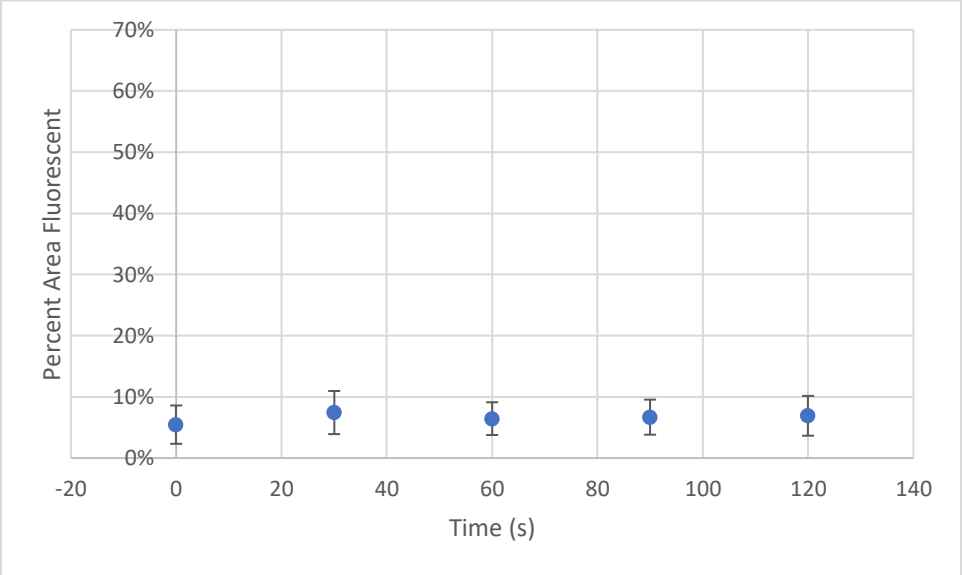


**Figure 4-15: Platelet adhesion at 1,000 $s^{-1}$ over time**

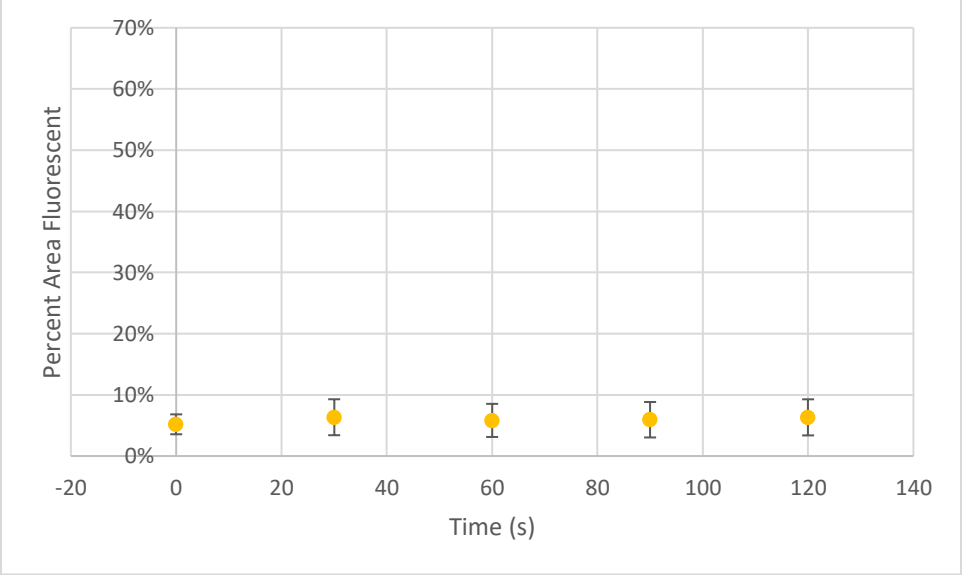


**Figure 4-16: Platelet adhesion at 1,5000 $s^{-1}$ over time.**

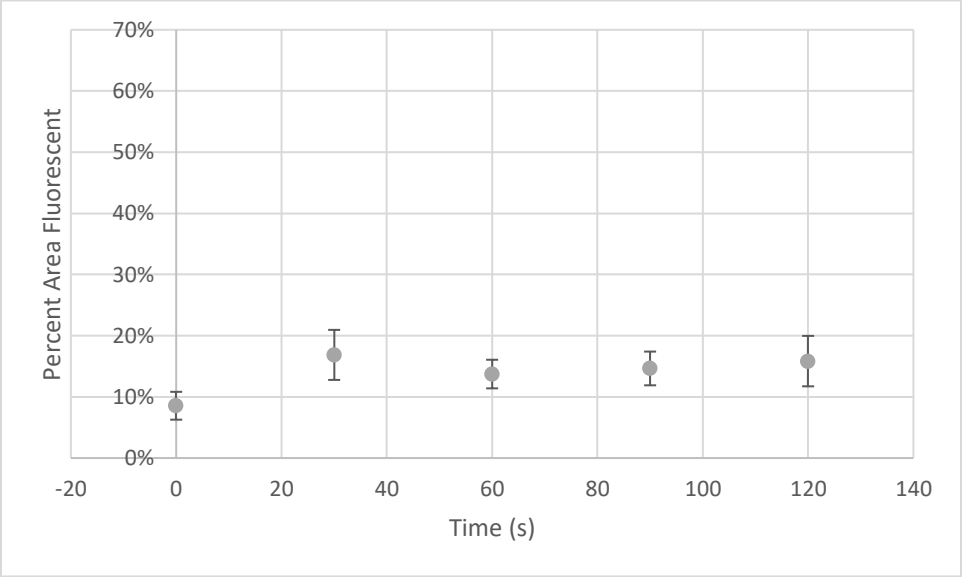


**Figure 4-17: Platelet adhesion at 3,333 $s^{-1}$ over time.**

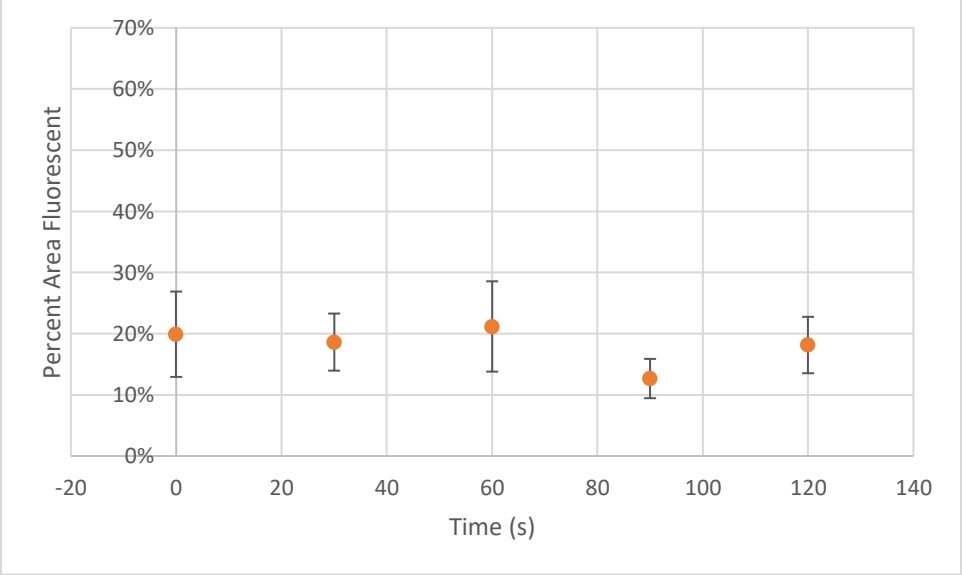


**Figure 4-18: Platelet adhesion at 5,000 $s^{-1}$ over time**

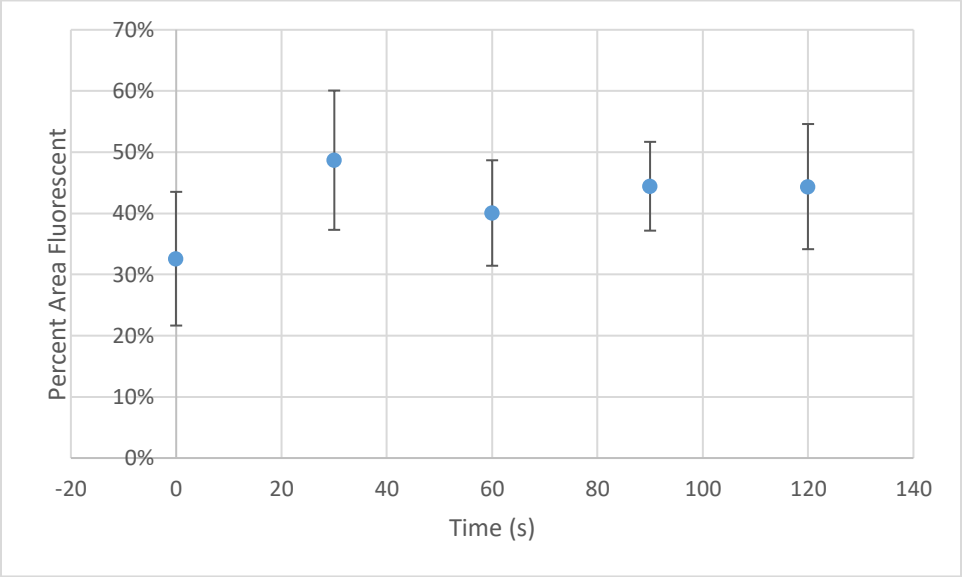


**Figure 4-19: Platelet adhesion at 10,000 $s^{-1}$ over time**

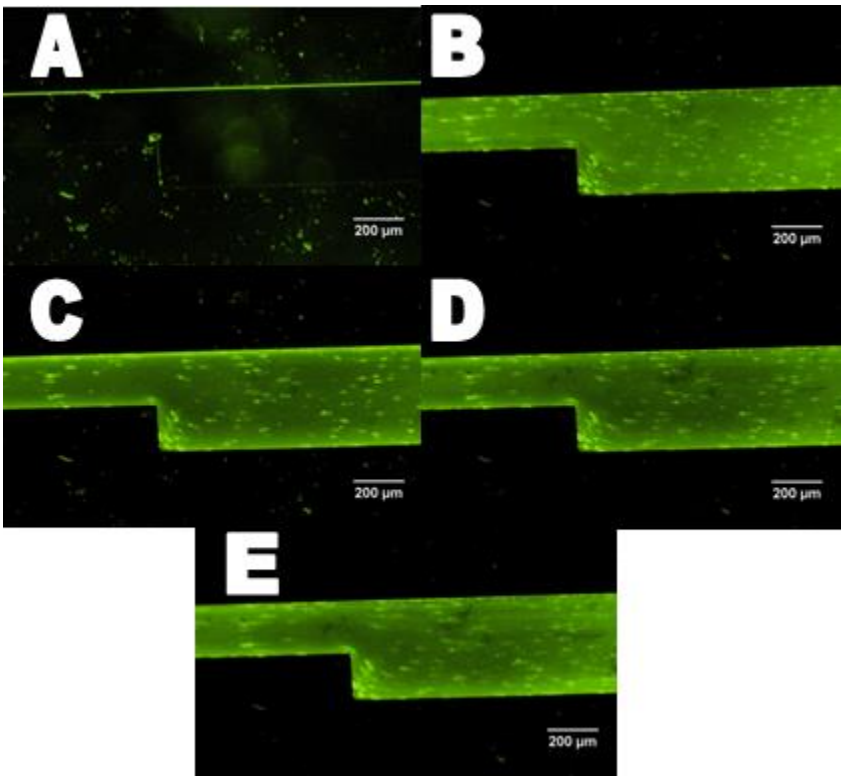


**Figure 4-20: Growth over time of platelets at 10,000 $s^{-1}$. Time points shown at (A) 0, (B) 30, (C) 60, (D) 90, and (E) 120 seconds.**

Figure 4-21 shows the data for various shear rates over time across the time points. At each time point 10,000 $s^{-1}$ has significantly more fluorescent area than all other rates. Fluorescence for 10,000 $s^{-1}$ is almost double the next closest shear condition at every time point after zero.

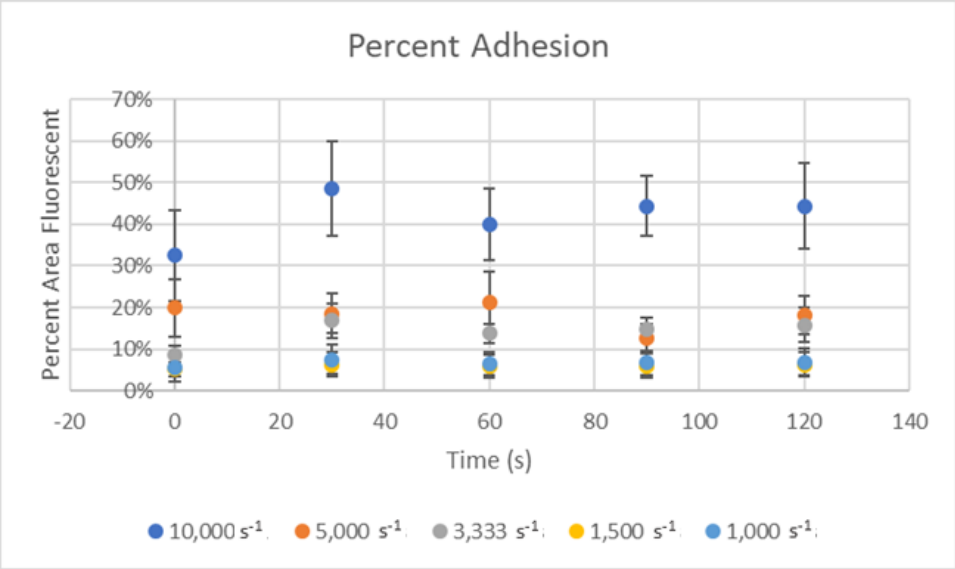


**Figure 4-21: Platelet adhesion over time for all 5 shear rate conditions.**

The percent area covered in fluorescence after the full two minutes is shown in Figure 4-22. A single factor ANOVA found that there were statistically significant differences in adhesion between groups ($p=0.00055$).

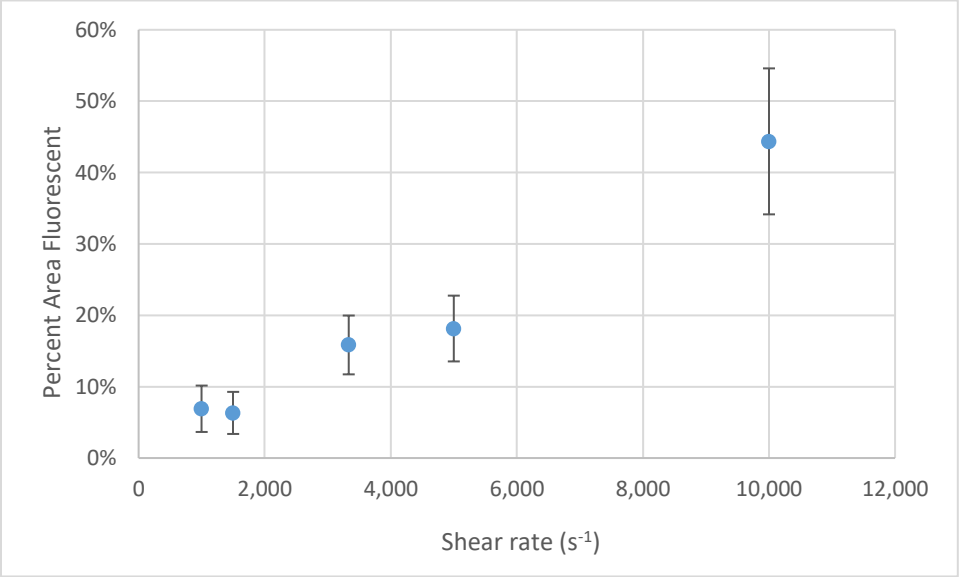


**Figure 4-22: Fluorescence coverage after two minutes of flow for all shear conditions.**

Figure 4-23 shows the adhesion of vWF at a variety of shear rates with and without ADAMTS-13 collected in previous studies. Figure 4-24 shows vWF adhesion and platelet adhesion, both without supplemented ADAMTS-13, normalized by their respective largest values.

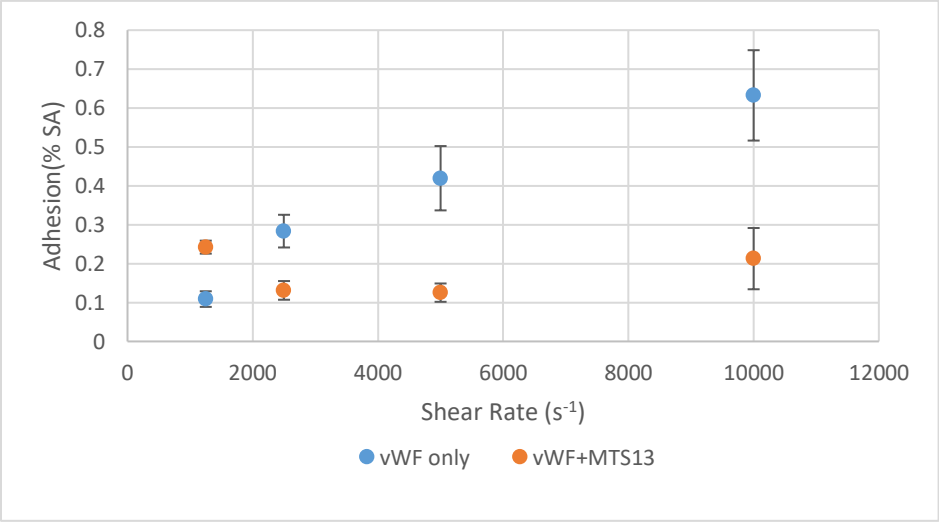


**Figure 4-23: vWF adhesion at varying shear rates for vWF and di$H_2O$. Means and standard deviation bars are shown.[47]**

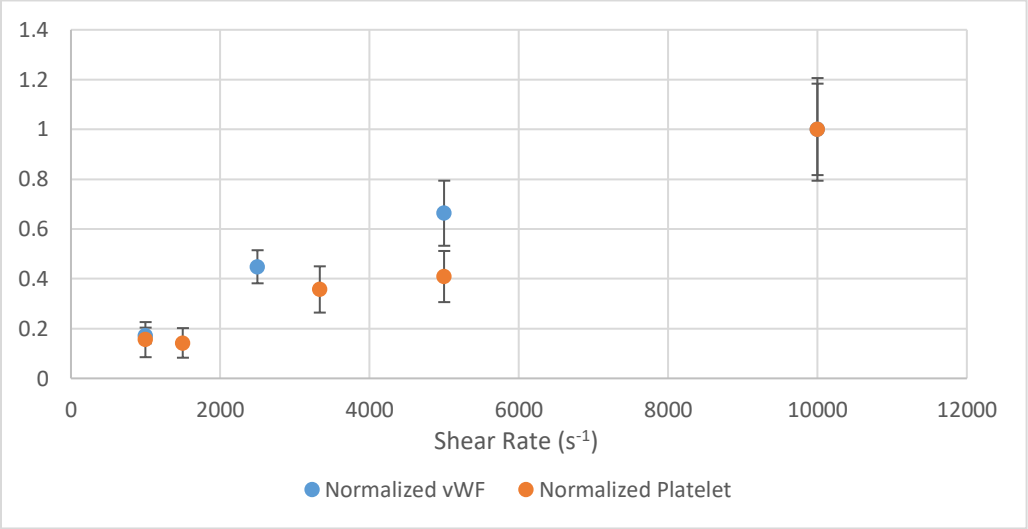


**Figure 4-24: Deposition of platelets and vWF [47] normalized by peak deposition.**

## ADAMTS-13 Effect on Platelets Direct IFM Experiment

Figures 4-25 through 4-27 show the progression of platelet deposition over 5 minutes for the three experimental shear rates. Averages and standard errors are shown for all time points collected. For 1,000 $s^{-1}$, the difference in fluorescence with and without ADAMTS-13 is not statistically significant at any time point (p=0.7912, 0.9088, 0.6804, 0.7736).

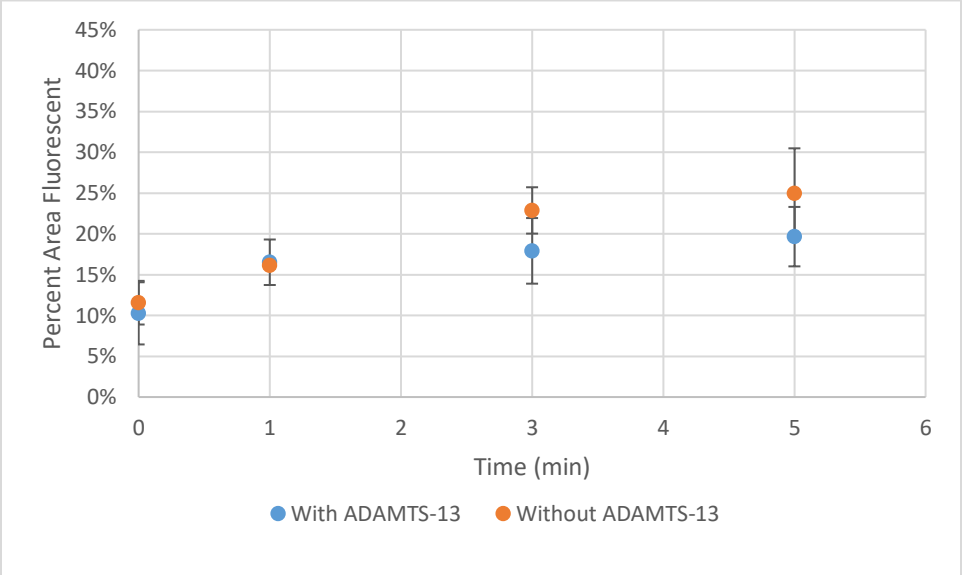


**Figure 4-25: Platelet deposition over time at 1,000 $s^{-1}$ with and without ADAMTS-13.**

For 5,000 $s^{-1}$, there is a significant difference in adherence at time points 1 min (p=0.0479) and 5 min (p=0.0004).

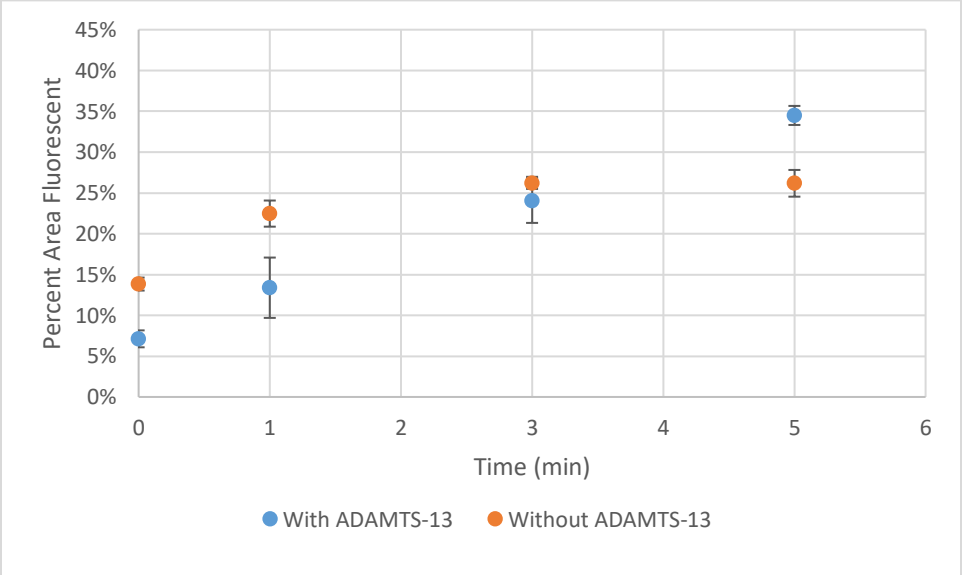


**Figure 4-26: Platelet deposition over time at 5,000 $s^{-1}$ with and without ADAMTS-13.**

For 10,000 $s^{-1}$, every time point past zero has a statistically significant difference in adhesion with and without ADAMTS-13 (t=1 min p=0.0032, t=3 min p=0.0185, t=5 min p=0.0004).

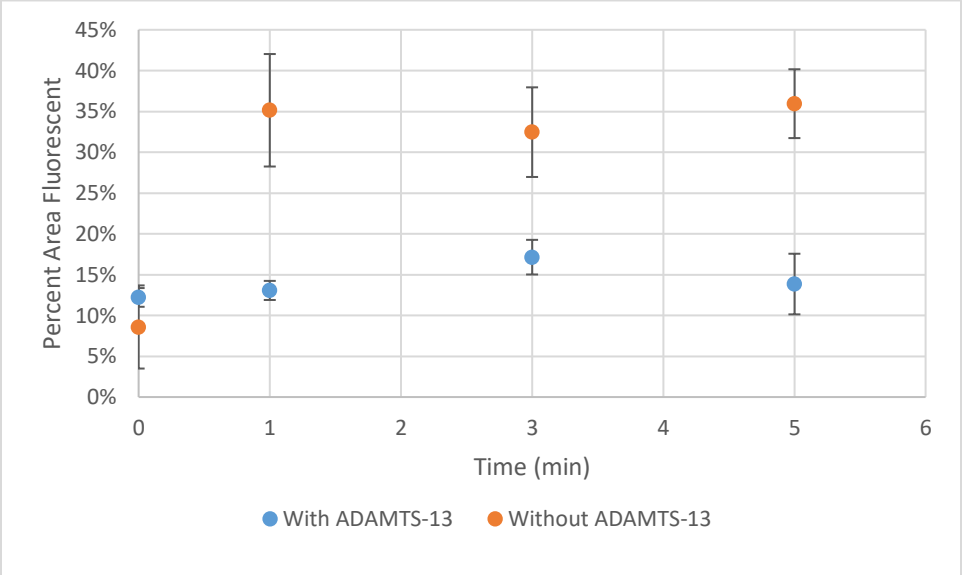


**Figure 4-27: Platelet deposition over time at 10,000 $s^{-1}$ with and without ADAMTS-13.**

Figure 4-28 shows the difference in adhesion due to the presence of ADAMTS-13 for all three shear rates after 5 minutes. According to a two factor ANOVA test, the interaction of shear rate and ADAMTS-13 results in statistically significant differences in adhesion ($p<0.001$).

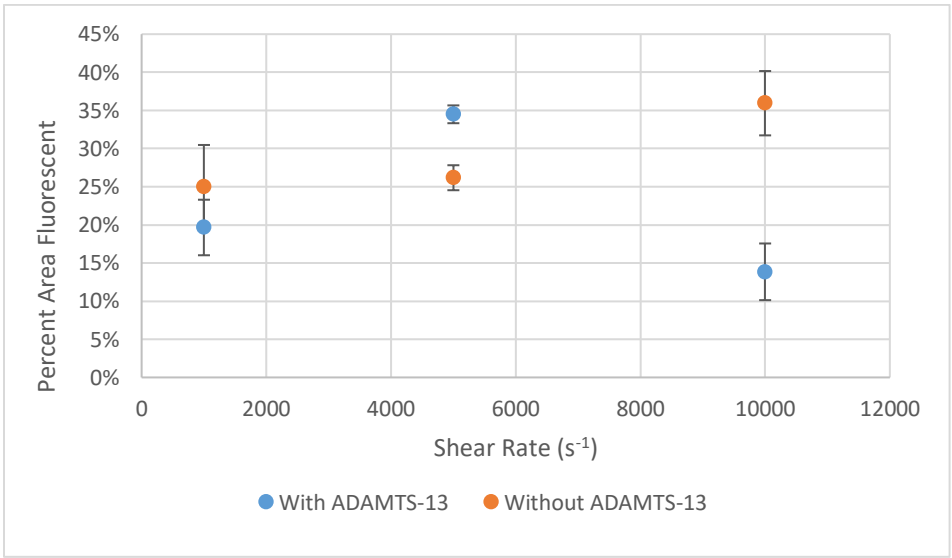


**Figure 4-28: Platelet deposition after two minutes for various shear rates with and without ADAMTS-13.**

# Chapter 5

# Discussion

## Micro Particle Image Velocimetry

For each flow rate, flow across the main channel of the crevice remains relatively consistent. Major changes in velocity occur at the crevice, however. The far corners within the crevice exhibit stagnation, remaining below 0.5 mm/s for all three flow rates. These areas of stagnation can cause increased risk of thrombus deposit in that region[54]. Flow at the inside corners of the crevice exhibit fast velocities as flow leaves and joins the main channel.

With increasing volumetric flow rate, the area of stagnation regions decreases showing that flow penetrates deeper into the crevice. Streamlines show that the far corners of the crevice are difficult to reach for fluid entering the crevice. For steady, laminar flow, particles in these regions could have trouble escaping. This leads to the possibility of small recirculation regions in these areas. If thrombosis were to occur in this region, it would be difficult to be washed away due to the low velocity.

Velocity vectors in the backward facing step are faster in the initial channel before the expansion. At the expansion, the far corner shows stagnation. As the fluid travels further from the expansion, flow across the channel begins to become more developed once again. Similar to the crevice, the area with flow slower than 0.5 mm/s decreases as the volumetric flow rate increases. Streamlines at the corners show that velocity vectors do not readily transport fluid into the corner. Resulting areas of stagnation could indicate risk for thrombosis[54].

When μPIV data was compared to the computational results, the values were within a small error range. These values validated the model used to calculate the average shear rate values for the channels under various flow conditions.

## Indirect Immunofluorescence Microscopy

In lower shear rates closer to physiological range, present in the medium and large channels, vWF adhesion for vWF in solution with di$H_2O$ remains fairly constant across shear rates. As the shear rate gets farther from physiological range in the small channel, vWF adhesion increases significantly. Somewhere between the shear rates 5,000 $s^{-1}$ and 10,000 $s^{-1}$, vWF adhesion hits a threshold where it begins to increase rapidly. LVAD-induced flow has shear rates greater than this, but the physiological range of shear rates ends within this range.

When ADAMTS-13 is included in solution, there is not an incline in deposition with shear as seen with isolated vWF in di$H_2O$. Across the three different channels, there was no significant change in adhesion. Due to the presence of ADAMTS-13, vWF adhesion does not spike after the threshold as it would without the cleaving enzyme. The consistency of vWF adhesion across the channels when ADAMTS-13 is present is likely due to the role it plays in regulating vWF. As high shear unravels the vWF, ADAMTS-13 cleaves the protein to regulate adhesion. In the high shear of LVAD flow, vWF needs to be cleaved significantly more to fall to this common level seen across different channels.

At all rates, a significant decrease in adhesion is seen with the addition of ADAMTS-13. This matches expectations because ADAMTS-13 acts as a cleavage enzyme and therefore works to decrease vWF size and adhesion[12]. The most severe decrease in adhesion occurred at the high shear rates. The high velocity flow in the small channels elongates the vWF revealing more cleavage sites[13]. The shear dependent unfurling and subsequent increase in number of exposed cleavage sites leads to the drastic decline in adhesion. If shear was to continue to increase to the upper limits of LVAD flow, near 100,000 $s^{-1}$, this unraveling would likely continue to increase and subsequent vWF cleavage would increase as well.

## Shear-Platelet Adhesion Direct IFM Experiment

When shear rates were increased to 10,000 $s^{-1}$, platelet adhesion appeared almost immediately in large quantities. For 1,000 $s^{-1}$ to 5,000 $s^{-1}$, there appears to be an increase in adhesion with an increase in shear rate. An increased sample size, and a larger range of shear rates, could provide better insight into this. After 5,000 $s^{-1}$, platelet deposition drastically increases with increased shear rate.

Figure 4-22 shows a trend in platelet deposition consistent with trends observed in vWF adhesion, shown in Figure 4-23. Figure 4-24 shows each data set normalized by the adhesion at 10,000 $s^{-1}$. In the normalized data, vWF and platelet adhesion follow a similar trend in adhesion with change in shear. This trend indicates that vWF and platelet adhesion are linked. Conditions with increased vWF adhesion also saw increased platelet deposition. As vWF adhesion increases, vWF interactions with GPIb increase allowing the slow rolling of platelets despite high shear. Increased interactions allow the platelets to form stable, more permanent bonds with the collagen mimicking a site of exposed extracellular matrix. This explains the increased platelet adhesion despite most platelet interactions becoming inefficient past 800 $s^{-1}$ [14]. The matching trends give evidence that vWF interactions are the primary driver for platelet adhesion at higher shear rates.

Due to the nature of real time imaging, a large amount of noise was present from unbound fluorescent dye flowing through the channel. To counteract the noise, various methods of processing and thresholding were used. More sophisticated techniques could be developed to help improve the signal to noise of the data.

## ADAMTS-13 Effect on Platelets Direct IFM Experiment

Analysis of platelet adhesion in the conditions of this experiment reveals some insight into the relationship between ADAMTS-13, vWF, and platelet adhesion. The consistency in adhesion at lower

shears in the presence of ADAMTS-13 and decrease at high shear rates gives evidence for different clotting mechanisms used to arrest platelets depending on shear. Previous studies have shown different thrombi characteristics based on shear rate likely due to the presence of different mechanisms leading to thrombus formation[48]. The findings of this study give further evidence to great differences in methods of platelet recruitment to injury sites based on shear rate.

At low shear rates, ADAMTS-13 did not significantly inhibit the adhesion of platelets. At lower shear rates, platelet adhesion is not entirely dependent on vWF adhesion to arrest platelets and begin primary hemostasis. Slow flow and margination allow platelet exposure to binding sites for sufficient time to create stable bonds [44]. Additionally, at these lower shear rates vWF function remains physiological, which slows platelet rolling further through continuous association and dissociation of A1-GPIb bonds [17,18].

At 10,000 $s^{-1}$, however, platelet adhesion in the presence of supplemented ADAMTS-13 led to a decrease in adhesion. This information, along with the similar trends in vWF and platelet adhesion previously discussed, alludes to the important role of vWF in high shear clotting. When vWF is increasingly adherent, platelets were as well. Flows at these speeds are too fast for the kinetics of platelet-collagen or platelet-fibrinogen interactions to form stable bonds without the help of vWF interactions. Even at speeds as high as 5,000 $s^{-1}$ platelet adhesion could persist because of help from vWF. In conditions where vWF would be significantly elongated, however, A2 cleavage sites would be revealed too often. The increased exposure of A2 domains in flow characteristic of LVADs explains the presence of low molecular weight vWF in LVAD patients. Thus, due to the lack of high molecular weight vWF multimers on collagen, platelet-vWF interactions cannot slow the platelets enough to arrest them at injury sites. Without the assistance of bound vWF to collagen, platelets have no interactions with kinetics fast enough to bind at time ranges limited by the rate of blood flow.

At 10,000 $s^{-1}$, platelet adhesion drops below that seen even at 1,000 $s^{-1}$. Thus, platelet adherence to collagen sites at these shear rates drops below that seen in physiological flow conditions. This demonstrates that high shear in the presence of ADAMTS-13 can inhibit the ability of platelets to be recruited and bind

to an injury site due to the protein's destruction of vWF multimers. These high shears, consistent with those seen in LVADs, prevent platelet aggregation due to increased cleavage of vWF, which could lead to bleeding episodes consistent with those seen in patients suffering from AVWS. Many areas of LVAD flow may even see shear rates much higher than those tested here[49]. These higher shears may further inhibit platelet recruitment due to increased vWF cleavage. The inability to initiate primary hemostasis due to absence of vWF-platelet rolling could explain the incidence of bleeding events.

The drop of adhesion below even 1,000 $s^{-1}$ due to vWF destruction at 10,000 $s^{-1}$ provides evidence that vWF-platelet interactions are a significant part of platelet adhesion even at higher physiological speeds. Without the presence of high molecular weight vWF, platelet adhesion cannot match adhesion at much lower speeds with functional vWF-platelet interactions. This is consistent with previous studies which found vWF function to be a primary contributor to platelet adhesion above 800 $s^{-1}$ [14].

At 5,000 $s^{-1}$, ADAMTS-13 presence increased surface area with adhered platelets. This could be due to the low sample size or high level of noise. Due to the high variability in platelet activity from person to person[52,53], a higher sample size should be tested at this condition to discern the validity of these effects.

The threshold for pathological shear which drastically inhibits platelet adhesion appears to be between 5,000 $s^{-1}$ and 10,000 $s^{-1}$. As seen in Figure 4-22, it is between these points that significant inhibition of adhesion is revealed. Further evidence of the presence of such a threshold near 5,000 $s^{-1}$ was seen qualitatively. Figure 5-1 shows an image taken for a shear rate of 5,000 $s^{-1}$ at the inlet. After the step, adhesion begins to significantly increase. The decreased shear rates allow vWF to furl up to protect cleavage sites in order to recruit platelet adhesion once more. The drop in adhesion after 5,000 $s^{-1}$ is consistent with previous studies finding the critical shear rate for vWF cleavage to be at 6,000 $s^{-1}$ [28,29]. A similar critical shear rate for platelet adhesion further justifies the hypothesis that decreased vWF adhesion leads to decreased platelet adhesion. Flow in peak shear regions of LVADs exhibiting rates above this critical shear rate leads to decreased ability to maintain hemostasis.

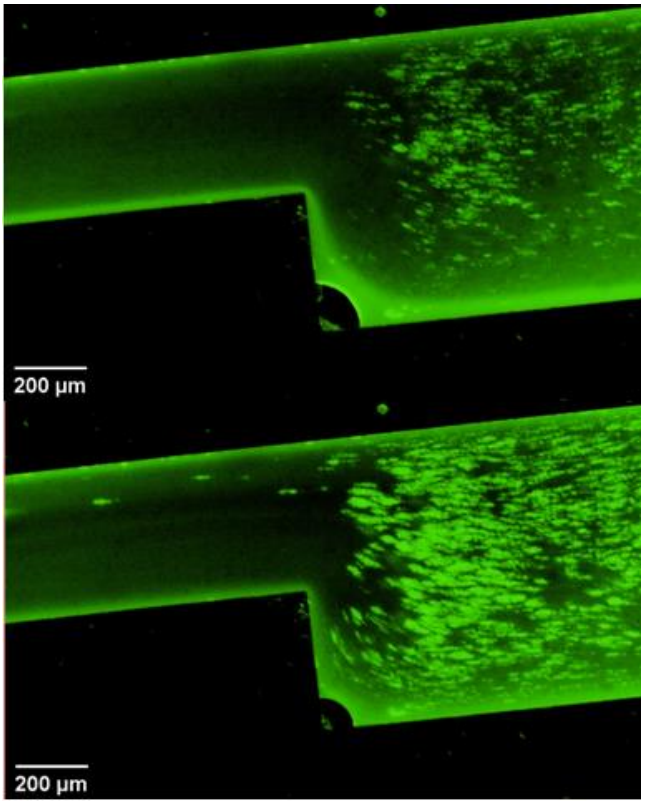


**Figure 5-1: Platelet adhesion at 3 minutes (top) and 5 minutes (bottom) for 50 µL/min flow in medium BFS.**

## Future Work

In the future, a larger sample size should be collected to add validation to the results and possibly provide a clearer insight into the dependence of platelet adhesion on shear at lower shear rates. Additional shear rates between 5,000 $s^{-1}$ and 10,000 $s^{-1}$, as well as higher VAD-like shear rates, should be collected to gain insight into the critical shear rate threshold for both increased deposition and pathological cleavage of vWF. Real time images of vWF deposition should be collected to supplement the indirect IFM images and the real time platelet images. In the future, images will be processed to understand the difference in adhesion at the entrance to the expansion, right after the expansion, and the far corner of the expansion. Particle sizes will also be determined to see the effect of ADAMTS-13 on vWF size and relative population of monomers and polymers.

## Appendix A

## Indirect IFM MATLAB Processing Code

```
%in ImageJ image adherence should be in white
%for new pictures, input image name, threshold, and pixel size

A=imread('image.tif'); %reads processed image
B=imbinarize(A); %creates matrix of binaries, 0=black 1=white
[c,d]=size(B);
percentarea=(sum(B,'all')/(c*d));%sums the white section (no adherence)...
%...and divides by image size

prompt='What is the pixel width?';
pixelsize=input(prompt); %prompts user to input pixel width
particles=bwconncomp(B); %analyzes particles by finding white objects
numparticles=particles.NumObjects; %extracts number of particles from...
%...particles structure

avgpixels=sum(B,'all')/numparticles; %average number of pixels per particle
avgarea=avgpixels*(pixelsize)^2; %converts average pixels to average area

mvpthresh=9; %minimum area of pixels for polymer

indpart=regionprops(B,'Area');%finds area of each particle
individparticles=transpose(cell2mat(struct2cell(indpart)));%converts...
%...structure into column vector

nummonomer=0;
numpolymer=0;
A=sort(individparticles)
for j=1:numparticles
   if individparticles(j,1) <= mvpthresh
      nummonomer=nummonomer +1; %when less than or equal to threshold...
      %...number of monomers increase
   else
      numpolymer=numpolymer +1; %if greater than threshold number ...
      %...of polymers increases
   end
end

disp(['The percent area with attachment is ', num2str(percentarea)])
disp(['The number of particles is ', num2str(numparticles)])
disp(['The number of monomers is ', num2str(nummonomer)])
disp(['The number of polymers is ', num2str(numpolymer)])
disp(['The average particle size is ', num2str(avgarea)])
imshow(B)
```

# BIBLIOGRAPHY


1. E.J. Benjamin, M.J. Blaha, S.E. Chiuve, et al. Heart disease and stroke statistics-2017 update: a report from the American Heart Association Circulation, 135 (2017), pp. 146-603
2. L. Miller, E. Birks, M. Guglin, H. Lamba, O.H. Frazier, "Use of Ventricular Assist Devices and Heart Transplantation for Advanced Heart Failure," *Circulation Research*, vol. 124, no. 11, pp. 1659–1678, May 2019.
3. Kormos RL, Cowger J, Pagani FD, Teuteberg JJ, Goldstein DJ, Jacobs JP, Higgins RS, Stevenson LW, Stehlik J, Atluri P, Grady KL, Kirklin JK. The society of thoracic surgeons intermacs database annual report: evolving indications, outcomes, and scientific partnerships. Ann Thorac Surg. 2019; 107:341–353. doi: 10.1016/j.athoracsur.2018.11.011
4. Lee, S.J., Kim, K.H., Hong, S.K. et al. Evaluation of a Heart Transplant Candidate. Curr Cardiol Rep 19, 133 (2017). https://doi.org/10.1007/s11886-017-0934-y
5. A. Kilic, S. Emani, C.B. Sai-Sudhakar, R.S. Higgins, & B.A. Whitson (2014). "Donor selection in heart transplantation," *Journal of thoracic disease*, vol. 6 no. 8, pp. 1097–1104, 2014 https://doi.org/10.3978/j.issn.2072-1439.2014.03.23
6. J.K. Kirklin, R. Xie, J. Cowger, T.M.M.H. de By, T. Nakatani, S. Schueler, R. Taylor, J. Lannon, P. Mohacsi, J. Gummert, D. Goldstein, K. Caliskan, M.M. Hannan, "Second annual report from the ISHLT Mechanically Assisted Circulatory Support Registry," The Journal of Heart and Lung Transplantation, vol. 37, no. 6, pp. 685–691, Jun. 2018.
7. Miller LW, Guglin M. Patient selection for ventricular assist devices: a moving target.J Am Coll Cardiol. 2013; 61:1209–1221. doi: 10.1016/j.jacc.2012.08.102
8. E. L. Wu, M. Kleinheyer, and A. Undar, "Pulsatile vs. continuous flow," in *Mechanical Circulatory and Respiratory Support*, Cambridge, MA: Academic Press, 2018, pp. 379–406.

9. C.R. Tainter, O.O. Braun, F. Teran, *et al.*Emergency department visits among patients with left ventricular assist devices Intern Emerg Med, 13 (2018), pp. 907-913
10. Imamura T, Kinugawa K, Uriel N. Therapeutic strategy for gastrointestinal bleeding in patients with left ventricular assist device. Circ J. 2018; 82:2931–2938. doi: 10.1253/circj.CJ-18-0883
11. E. W. Davie, K. Fujikawa, and W. Kisiel, "The coagulation cascade: initiation, maintenance, and regulation," *Biochemistry*, vol. 30, no. 43, pp. 10363–10370, Oct. 1991.
12. P. Tunney, "Interpreting Coagulation Studies," *MedSchool*, 22-Oct-2020. [Online]. Available: https://medschool.co/tests/coag/interpreting-coagulation-studies. [Accessed: 15-Nov-2020].
13. K. South and D.A. Lane, "ADAMTS-13 and von Willebrand factor: a dynamic duo," *Journal of Thrombosis and Haemostasis*, vol. 16, pp. 6-18, 2018.
14. V. Huck, M. F. Schneider, C. Gorzelanny, and S. W. Schneider, "The various states of von Willebrand factor and their function in physiology and pathophysiology," *Thrombosis and Haemostasis*, vol. 111, no. 4, pp. 598–609, 2014.
15. Peyvandi, F., Garagiola, I., & Baronciani, L. Role of von Willebrand factor in the haemostasis. *Blood transfusion*, 9 Suppl 2(Suppl 2), s3–s8, 2011.
16. C.R. Bartoli, D.J. Restle, D.M. Zhang, M.A. Acker, P. Atluri, "Pathologic von Willebrand factor degradation with a left ventricular assist device occurs via two distinct mechanisms: Mechanical demolition and enzymatic cleavage," *Journal of Thoracic and Cardiovascular Surgery*, vol. 149, no. 1, pp. 281–289, Jan. 2015.
17. F. Denorme, K. Vanhoorelbeke, and S. F. De Meyer, "von Willebrand Factor and Platelet Glycoprotein Ib: A Thromboinflammatory Axis in Stroke," *frontiers in Immunology*, vol. 10, no. 2884, Dec. 2019.
18. Initiation of Platelet Adhesion by Arrest onto Fibrinogen or Tranlocation on vWF

19. A.L. Meyer, D Malehsa, U Budde, C Bara, A Haverich, M Strueber, “Acquired von Willebrand Syndrome in Patients With a Centrifugal or Axial Continuous Flow Left Ventricular Assist Device,” *JACC: Heart Failure*, vol. 2, no. 2, pp. 141–145, 2014.
20. S. Crow, R. John, A. Boyle, et al. Gastrointestinal bleeding rates in recipients of nonpulsatile and pulsatile left ventricular assist devices J Thorac Cardiovasc Surg, 137 (2009), pp. 208-215
21. N. Uriel, S. Pak, U.P. Jorde, B. Jude, S. Susen, A. Vincentelli, P. Ennezat, S. Cappleman, Y. Naka, D. Mancini, “Acquired von Willebrand Syndrome After Continuous-Flow Mechanical Device Support Contributes to a High Prevalence of Bleeding During Long-Term Support and at the Time of Transplantation,” *Journal of the American College of Cardiology*, vol. 55, no. 15, pp. 1207–1213, Oct. 2010.
22. A.L. Meyer, D. Malehsa, C. Bara, et al. “Acquired von Willebrand syndrome in patients with an axial flow left ventricular assist device,” *Circ Heart Fail*, vol. 3, pp. 675-681, 2010.
23. S. Crow, D. Chen, C. Milano, et al. “Acquired von Willebrand syndrome in continuous-flow ventricular assist device recipients,” *Ann Thorac Surg*, 90, pp. 1263-1269, 2010.
24. A. Vincentelli, S. Susen, T. Le Tourneau, et al. Acquired von Willebrand syndrome in aortic stenosis N Engl J Med, 349 (2003), pp. 343-349
25. C.R. Bartoli, J.Kang, D. Zhang, J. Howard, M. Acker, P. Atluri, MD, and T Motomura, “Left Ventricular Assist Device Design Reduces von Willebrand Factor Degradation: A Comparative Study Between the HeartMate II and the EVAHEART Left Ventricular Assist System,” *Annals of Thoracic Surgery*, vol. 103, pp. 1239–1245, 2017.
26. Harkins, T. (2019). *Development of a Micro-Particle Image Velocimetry Platform to Study Thrombosis* in vitro [Unpublished Bachelor’s Thesis]. The Pennsylvania State University.
27. Gurvits, Grigoriy E, and Elena Fradkov. “Bleeding with the artificial heart: Gastrointestinal hemorrhage in CF-LVAD patients.” *World journal of gastroenterology*, 23,22 (2017), pp. 3945-3953.

28. S. Lippok, M. Radtke, T. Obser, L. Kleemeier, R. Schneppenheim, U. Budde, R. R. Netz, and J. O. Rädler, “Shear-Induced Unfolding and Enzymatic Cleavage of Full-Length VWF Multimers,” *Biophysical Journal*, vol. 110, no. 3, pp. 545–554, Feb. 2016.
29. C. H. Chan , M. Inoue , K. K. Ki, T. Murashige , J. F. Fraser , M. J. Simmonds , G. D. Tansley , and N. Watanabe, “Shear-dependent platelet aggregation size,” *Artificial Organs*, Jul. 2020.
30. O. O. Ilesanmi, “Pathological basis of symptoms and crises in sickle cell disorder: implications for counseling and psychotherapy,” *Hematology Reports*, vol. 2, no. 1, Apr. 2010.
31. A. Yazdani , H. Li, J. D. Humphrey, and G. E. Karniadakis, “A General Shear-Dependent Model for Thrombus Formation,” *Plos Computational Biology*, vol. 13, no. 1, Jan. 2017.
32. R. Chaudhry, S.M. Usama, H.M. Babiker. Physiology, Coagulation Pathways. [Updated 2020 Sep 3]. In: StatPearls [Internet]. Treasure Island (FL): StatPearls Publishing; 2020 Jan-. Available from: https://www.ncbi.nlm.nih.gov/books/NBK482253/
33. S. P. Grover and N. Mackman, “Tissue factor,” *Atherosclerosis, Thrombosis, and Vascular Biology*, vol. 38, no. 4, pp. 709–725, Feb. 2018.
34. S. P. Grover and N. Mackman, “Intrinsic Pathway of Coagulation and Thrombosis,” *Arteriosclerosis, Thrombosis, and Vascular Biology*, vol. 39, no. 3, pp. 331–338, Jan. 2019.
35. J. F. Vojacek, “Should We Replace the Terms Intrinsic and Extrinsic Coagulation Pathways With Tissue Factor Pathway?,” *Clinical and Applied Thrombosis/Hemostasis*, vol. 23, no. 8, pp. 922–927, Oct. 2016.
36. S.-H. Yun, E.-H. Sim, R.-Y. Goh, J.-I. Park, and J.-Y. Han, “Platelet Activation: The Mechanisms and Potential Biomarkers,” *BioMed Research International*, vol. 2016, pp. 1–5, Jun. 2016.

37. J. Qiao, J. F. Arthur, E. E. Gardinere, R. K. Andrews, L. Zeng, and K. Xu, “Regulation of platelet activation and thrombus formation by reactive oxygen species,” *Redox Biology*, vol. 14, pp. 126–130, Apr. 2018.
38. K. Harter, M. Levine, and S. O. Henderson, “Anticoagulation Drug Therapy: A Review,” *Western Journal of Emergency Medicine*, vol. 16, no. 1, pp. 11–17, Jan. 2015.
39. W. Ageno, A. S. Gallus, A. Wittkowsky, M. Crowther, E. M. Hylek, and G. Palareti, “Oral Anticoagulant Therapy,” *Chest*, vol. 141, pp. e44S–e88S, Feb. 2012.
40. A. Milionis, I. S., D. Fragouli, F. Brandi, and A. Athanassiou, “Combination of Lithography and Coating Methods for Surface Wetting Control,” *Updates in Advanced Lithography*, 2013.
41. M. Kalashnikova, J. Campbell, M. Knoch, I. Hanelta, K. Sahagian, A. Sharon, and A. Sauer-Budge, “Plasma-assisted building and coating of multi-layered microfluidic devices.” Fraunhofer, USA.
42. M. Raffel, C. E. Willert, F. Scarano, C. J. Kähler, S. T. Wereley, and J. Kompenhans, “Micro-PIV,” in *Particle Image Velocimetry*, Berlin, Germany: Springer, 2018, pp. 367–411.
43. S. Gregersen, “Flourescent peptide-stabilized silver-nanoclusters: a solid-phase approach for high-throughput ligand discovery,” thesis, København, 2014.
44. A. Jain, A. D. D. van der Meer, A.-L. Papa, R. Barrile, A. Lai, B. L. Schlechter , M. A. Otieno, C. S. Louden, G. A. Hamilton, A. D. Michelson, A. L. Frelinger III , and D. E. Ingber, “Assessment of whole blood thrombosis in a microfluidic device lined by fixed human endothelium,” *Biomedical Microdevices*, vol. 18, no. 73, Jul. 2016.
45. C. M. Thomazini, R. D. P. S. Soares, T. R. F. D. Rocha, A. T. A. Sachetto, and M. L. Santoro, “Optimization of von Willebrand factor multimer analysis in vertical mini-gel electrophoresis systems: A rapid procedure,” *Thrombosis Research*, vol. 175, pp. 76–83, Mar. 2019.
46. E. I. Oduah, R. J. Linhardt, and S. T. Sharfstein , “Heparin: Past, Present, and Future,” *Pharmaceuticals*, vol. 9, no. 3, Jul. 2016.

47. Watson, C., Rizzo, S., Ward, S., Redaelli, A., & Manning, K. (2021, July 11). *Inhibition of the Adhesive Behavior of von Willebrand Factor Due to Enzymatic Cleavage.* Poster presented at 26th Congress of the European Society of Biomechanics.

48. M. Lui, E. E. Gardiner, J. F. Arthur, I. Pinar, W. M. Lee, K. Ryan J. Carberry, & R. K. Andrews, "Novel Stenotic Microchannels to Study Thrombus Formation in Shear Gradients: Influence of Shear Forces and Human Platelet-Related Factors," *International journal of molecular sciences*, vol. 20, no. 12, 2019.

49. G. Rosenberg, C. A. Siedlecki, C.-S. Jhun, W. J. Weiss, K. Manning, S. Deutsch, and W. Pierce, "Acquired Von Willebrand Syndrome and Blood Pump Design," *Artificial Organs,* vol. 42, no. 12, pp. 1119–1124, 2018.

50. B.P. Selgrade, and G.A. Truskey, "Computational fluid dynamics analysis to determine shear stresses and rates in a centrifugal left ventricular assist device," *Artificial Organs,* vol. 36, no. 4 pp. 89-96, 2012.

51. J. J. Dumas, R. Kumar, T. McDonagh, M. L. Stahl, W. S. Somers, "Crystal Structure of the Wild-type von Willebrand Factor A1-Glycoprotein Ibα Complex Reveals Conformation Differences with a Complex Bearing von Willebrand Disease Mutations," *Journal of Biological Chemistry*, vol. 279, no. 22, pp. 23327-23334, May 2004.

52. G. Lesyk and P. Jurasz, "Advances in Platelet Subpopulation Research," *Front. Cardiovasc. Med*. vol. 6, 2019.

53. S. Karpatkin, "Heterogeneity of human platelets. I. Metabolic and kinetic evidence suggestive of young and old platelets," *J. Clin. Invest* vol. 48, pp. 1073–1082, 1969.

54. A.R. Prisco, A. Aliseda, J.A. Beckman, N.A. Mokadam, C. Mahr, G.J.M Garcia, "Impact of LVAD Implantation Site on Ventricular Blood Stagnation," *ASAIO J*. vol. 63, no. 4, pp. 392-400, 2017.

**ACADEMIC VITA**

# Shane Ward

## EDUCATION

**The Pennsylvania State University** — **University Park, PA**
**Schreyer Honors College**
*Bachelor of Science in Biomedical Engineering* — *August 2017- May 2021*
**Politecnico di Milano** — **Milan, Italy**
Semester Abroad — *February 2020 - July 2020*

## WORK EXPERIENCE

**Artificial Heart and Cardiovascular Fluid Dynamics Lab** — **University Park, PA**
*Undergraduate Research Assistant* — *January 2019 - Present*

- Study von Willebrand factor binding under varying shear in microfluidic devices using immunofluorescence
- Study areas of thrombosis in geometric irregularities using Micro-Particle Image Velocity
- Fabrication of hundreds of PDMS microfluidic channels in cleanroom environment
- Live staining of platelets and von Willebrand factor in whole blood for hemodynamic studies

*Summer Translational Cardiovascular Science Institute* — *May 2019 - August 2019*
**The Pennsylvania State University** — **University Park, PA**
*Learning Assistant – Fundamentals of Cells and Molecules* — *January 2021 – Present*

- Assist students in learning through twice a week office hours

*Learning Assistant -- Biothermodynamics* — *August 2020 – December 2020*

- Facilitate weekly hour-long lecture reviews while assisting students on concepts from the given material
- Support in the assessment of exams and assignments of ninety students

## TECHNICAL SKILLS

*Languages*: MATLAB
*Software:* SolidWorks, COMSOL, Ansys Fluent, Abaqus FEA, Mimics, Insight, Tecplot
*Techniques:* Soft Lithography, micro-Particle Image Velocimetry, Cell Culture

## ABSTRACTS

Inhibition of the Adhesive Behavior of von Willebrand Factor Due to Enzymatic Cleavage, Spring 2021 – Investigating the role of vWF on adhesion on biomaterials and the modulating effects of ADAMTS-13, specifically in relation to thrombosis mediated by implanted devices. [Submitted to ESB 2021 Annual Meeting]

Thrombogenic Activity of von Willebrand Factor Under Shear on Biological Substrates in a Microfluidic Device, Spring 2021 – Studying the effect of shear rate on the adhesive behavior of vWF on biomaterials, leading to novel strategies to reduce device mediated thrombosis. [Submitted to ASIAO 2021 Annual Meeting]

## CAMPUS INVOLVEMENT

**Tau Beta Pi, Honors Society** — **State College, PA**
*Member* — *September 2020 - Present*
**Pennsylvania State University Rotor Act** — **State College, PA**
*Member* — *September 2020 - Present*
**Penn State THON** — **State College, PA**
*TREE Chair/Sustainability Liaison* — *October 2017 - February 2019*